# OPTICAL PROPERTIES OF NANOPARTICLES THIN FILM IN ORGANIC LIGHT EMITTING DIODE (OLED)

SITI MUNIRAH BINTI CHE NOH

FACULTY OF SCIENCE
UNIVERSITY OF MALAYA
KUALA LUMPUR

2017

# OPTICAL PROPERTIES OF NANOPARTICLES THIN FILM IN ORGANIC LIGHT EMITTING DIODE (OLED)

SITI MUNIRAH BINTI CHE NOH

DISSERTATION SUBMITTED IN FULFILMENT OF THE REQUIREMENTS FOR THE DEGREE OF MASTER OF SCIENCE

DEPARTMENT OF PHYSICS
FACULTY OF SCIENCE
UNIVERSITY OF MALAYA
KUALA LUMPUR

2017

# UNIVERSITY OF MALAYA
# ORIGINAL LITERARY WORK DECLARATION

Name of Candidate: **Siti Munirah Binti Che Noh**

Matric No: **SGR120006**

Name of Degree: **Master of Science**

Title of Project Paper/Research Report/Dissertation/Thesis (“this Work”): **OPTICAL PROPERTIES OF NANOPARTICLES THIN FILM IN ORGANIC LIGHT EMITTING DIODE (OLED)**

Field of Study: **Experimental Physics**

I do solemnly and sincerely declare that:

(1) I am the sole author/writer of this Work;
(2) This Work is original;
(3) Any use of any work in which copyright exists was done by way of fair dealing and for permitted purposes and any excerpt or extract from, or reference to or reproduction of any copyright work has been disclosed expressly and sufficiently and the title of the Work and its authorship have been acknowledged in this Work;
(4) I do not have any actual knowledge nor do I ought reasonably to know that the making of this work constitutes an infringement of any copyright work;
(5) I hereby assign all and every rights in the copyright to this Work to the University of Malaya (“UM”), who henceforth shall be owner of the copyright in this Work and that any reproduction or use in any form or by any means whatsoever is prohibited without the written consent of UM having been first had and obtained;
(6) I am fully aware that if in the course of making this Work I have infringed any copyright whether intentionally or otherwise, I may be subject to legal action or any other action as may be determined by UM.

Candidate’s Signature                Date: 3rd August 2017

Subscribed and solemnly declared before,

Witness’s Signature                Date: 3rd August 2017

Name: DR ROZALINA BINTI ZAKARIA

Designation: SENIOR LECTURER

# ABSTRACT

In-depth study on silver nanoparticles (Ag) has been conducted through UV-Visible (UV-Vis) spectroscopy, atomic force microscopy (AFM), field emission scanning electron microscopy (FESEM), and current-brightness-voltage (IVL) measurement. A thin layer of silver nanoparticles was produced by depositing silver thin film on top of indium tin oxide (ITO) substrate via electron beam (e-beam) deposition system. Nanoparticles formed through self-assemble dewetting process after annealing treatment in furnace with temperature ranging from 200 $^{o}$C to 400 $^{o}$C, which yields different sizes of nanoparticles. The obtained results were used as training and checking data input for soft computing methodology Support Vector Regression (SVR). The SVR was used for estimation of sizes of nanoparticles formed on top of substrate at certain temperatures. The experimental results show an improvement in predictive accuracy and capability of generalization which can be achieved by the SVR_poly approach in compare to SVR_rbf and SVR_lin methodology. Estimation of local surface plasmon resonance (LSPR) over a broad wavelength range is simulated using an adaptive neurofuzzy inference system (ANFIS) method. The ANFIS methodology allows for estimation of sizes of granular structures formed on top of a substrate at certain temperatures, whereupon these intelligent estimators are implemented using MATLAB and their subsequent performances are investigated. The results presented in this thesis work show the effectiveness of the method of simulation. The plasmonic effect of Ag NPs with remarkable optical properties lead us to integrate the particles in the red and green phosphorescent organic light emitting diodes (OLED) as hole injection layer (HTL). The device with Ag NPs layer achieved more than 3 folds enhancement compared to the device without Ag NPs.

# ABSTRAK

Kajian mendalam mengenaik zarah nano perak (Ag NP) telah dijalankan melalui daya atom mikroskop (AFM), mikroskopi pengimbasan pelepasan elektron (FESEM), ukuran arus-cahaya-voltan (IVL) dan UV-Vis (UV-Vis) spektroskopi. Satu lapisan nipis zarah nano perak telah dihasilkan dengan mendepositkan filem nipis perak di atas substrat oksida indium timah (ITO) menggunakan alur elektron (e-beam) sistem pemendapan. Zarah nano dibentuk melalui proses pembentukan kendiri selepas dipanaskan dalam relau dengan suhu antara 200 $^{o}$C untuk 400 $^{o}$C yang menghasilkan saiz zarah nano yang berbeza. Keputusan yang diperolehi digunakan sebagai latihan dan memeriksa kaedah pengkomputeran Support Vector Regresi (SVR). SVR digunakan untuk menganggar saiz nanopartikel yang terbentuk di atas substrat pada suhu tertentu. Keputusan eksperimen menunjukkan peningkatan dalam ketepatan dan keupayaan generalisasi yang boleh dicapai dengan pendekatan SVR_poly di bandingkan dengan kaedah SVR_rbf dan SVR_lin ramalan. Anggaran resonan plasmon tempatan dalam julat panjang gelombang yang luas disimulasi menggunakan sistem kaedah penyesuaian neurofuzzy inferens (ANFIS). Kaedah ANFIS membolehkan anggaran saiz struktur berbutir terbentuk di atas substrat pada suhu tertentu, di mana ini penganggar bijak dilaksanakan menggunakan MATLAB dan persembahan berikutnya disiasat. Keputusan yang dibentangkan dalam kerja ini menunjukkan keberkesanan kaedah simulasi. Efek plasmonik pada Ag NPs ini membenarkan kami untuk mengintegrasikan zarah dalam peranti cahaya organik diod pemancar (OLED) berwarna merah dan hijau sebagai lapisan memasukkan 'hole' (HIL). Peranti yang menggunakan Ag NP menunjukkan peningkatan lebih daripada 3 kali ganda peningkatan diperolehi berbanding peranti tanpa Ag NP.

# ACKNOWLEDGEMENTS

First of all, I thank Allah the Almighty for all His providence in carrying out this work successfully.

I would like to express my deepest gratitude to my supervisors Dr. Rozalina Zakaria and Dr. Woon Kai Lin for guidance, support, patience and encouragement throughout the course of this work.

I am grateful and touched for the attentions and support from my loving husband, Mohd Kamil bin Ramli. I am blessed to have you and our daughter in my life. I am indebted to my late father Che Noh Mat Il and my mother Samsiah binti Awang, for their constant encouragement and understanding throughout the years of my life. Hereby, I place on record to dedicate this thesis solely to my beloved parents and husband.

Also, my warm thanks to my fellow labmates in for the stimulating discussions, for the struggle we have in working together before deadlines and for all the fun we have had. Special thanks to Noor Azrina Talik and Khairus Syifa Hamdan for all the helps and supports.

Last but not least, my sense of gratitude to one and all, who directly or indirectly have lent their hand in this venture.

# TABLE OF CONTENTS

## LIST OF FIGURES

# LIST OF TABLES

# CHAPTER 1: INTRODUCTION

## 1.1 Introduction

When the size of a matter is reduced from bulk to the nanometer scale, the new properties will emerge. These significant new properties, such as optical, electronic, surface and structural properties make nano-size particles are manipulated for various applications such as signal amplifications, light trapping in light emitting device, light guiding and focusing, sensors, and a lot more.

Since 1908, scientist has figured out the existence of surface plasmons (Gaspar et al., 2013) which occurs when light (electromagnetic wave) strikes on noble metal nanoparticles and results in collective oscillation of free electrons. Noble metals such as gold (Au) and silver (Ag) is denoted as plasma in Drude-Lorentz model because it contains equal numbers of positive ion (fixed in positions) and conductive electrons (free and highly mobile). However, silver was chosen in this work since it is cheaper compared to gold.

Manufacturers are looking for simple, time and cost effective technique that can produce nanoparticles easily. Scientist has found that a process called dewetting occurred when the thin liquid film on the substrate ruptured due to application of heat and formed droplets.

## 1.2 Motivations and Objectives

The objectives of the research work presented in this thesis are:

1. to study the influence of size and thickness of silver nanoparticles towards the optical properties.
2. to verify the compatibility between the simulation and experimental's result.

3. to fabricate OLED device using silver nanoparticles in order to observe the influence of SPR in OLED efficiency.

## 1.3 Thesis outline

This thesis covers six chapters that discuss the optical properties of silver nanoparticles, produced by simple and cost-effective technique which then applied in Organic Light Emitting Diodes (OLED) to observe the effects in device efficiency. The overview of the plasmonics and OLED research has been done to date and briefly discussed in Chapter 2.

Following that, in Chapter 3 focuses on the experimental techniques that has been carried out in this work. The mechanism of machine that were used and OLED device fabrication process are discussed in details.

The results obtained from this study are presented in two different chapters, Chapter 4 and 5. Chapter 4 reveals the temperature and thickness effect of silver nanoparticles towards Surface Plasmon Resonance (SPR). Morphological characterizations using FESEM and AFM, and optical characterizations using UV-Vis are discussed. Support vector regression (SVR) method for the SPR prediction, Adaptive Neuro-Fuzzy Inference System (ANFIS) simulation result and their analysis are also presented in this chapter.

Chapter 5 shows green and red electrophosphorescent OLED device together with the plasmonic properties of the nanoparticles incorporated in the device which is the SPR peak obtained from UV-Vis Spectroscopy.

Consolidation of the conclusions drawn out from the present work is reported in Chapter 6. Suggestions for future studies are also indicated.

# CHAPTER 2: BACKGROUND THEORY AND LITERATURE REVIEW

## 2.1 Nanoparticles: historical perspectives

Metal nanoparticles have exciting optical properties. "Ruby glass", which is essentially glass containing gold nanoparticles, has been used since ancient time until the present. A classic example of an ancient piece of art gaining its appeal from the color produced by metal nanoparticles is the late Roman "Lycurgus Cup", which is exhibited in the British Museum. Figure 2.1 shows the stunning effect is due to absorption and scattering of gold nanoparticles, which are present in the glass from which the cup is made (Daniel & Astruc, 2004).

**Figure 2.1:** Roman "Lycurgus Cup" with gold nanoparticles (adapted from Freestone, Meeks et al., 2007).

Garnett and Gustav Mie independently described the interaction of metallic nanoparticles with light and restructured the observed nanoparticle colors using classical electromagnetism. This classical description of light absorption and scattering by metal nanoparticles still being implemented today and is a foundation of successful scientific discoveries (Daniel & Astruc, 2004).

## 2.2 Nanoparticles productions

There are various way of producing nanoparticles have been reported and can be divided in two parts; top-down and bottom-up. Top-down means starting with a bulk material and then break it into smaller pieces using mechanical, chemical or other form of energy for examples, lithography (Hulteen et al., 1999), photolithography (Sun et al., 2006), electron-beam lithography (Mendes et al.,, 2004), macro-machining (eg; femto-second laser (Eliezer et al., 2004) and focused ion beam (FIB)). Bottom-up is an opposite approach, where materials are synthesized from atomic or molecular species via chemical reactions, allowing for the particles to grow in sizes. Metal-organic chemical vapour deposition (MOCVD) (Shah et al., 2002), plasma-enhanced chemical vapour deposition (PECVD) (Delachat et al., 2009) and electron beam deposition (Zakaria et al., 2014; Zakaria et al., 2012) are the examples of bottom-up techniques. Both approaches can be done in either gas, liquid, supercritical fluids, solid states, or in vacuum. Most of the researches and manufacturers are interested in the ability to control particle size, particle shape, size distribution, particle composition and degree of particle agglomeration.

Self-assembly with dewetting process was used in this work where substantial amount of silver nanoparticles at reasonably low-cost have been produced. Solid silver thin films, produced by electron beam deposition are usually metastable or unstable in the as-deposited state, and they will dewet or agglomerate to form islands when heated to adequately high temperatures. This process is driven by surface energy minimization and can occur via surface diffusion well below a film's melting temperature, especially when the film is very thin (Thompson, 2012). Dewetting can also be useful in making arrays of nanoscale particles for electronic and photonic devices and for catalysing growth of nanotubes and nanowires. Templating of dewetting using patterned surface topography or pre-patterning of films can be used to create ordered arrays of particles and complex patterns of partially dewetted structures.

## 2.3 Variations of nanostructures

Various shapes of nanoparticles can be developed in our growing technologies and latest equipment. Nanotubes, nanowires, nanobelts, nanoflowers, nanoparticles, nanoflakes and nanofoams are examples of types of nanostructure. The geometry of the nanostructure (Figure 2.2) itself can be created and modified, depending on the techniques that were used and the parameters involved.

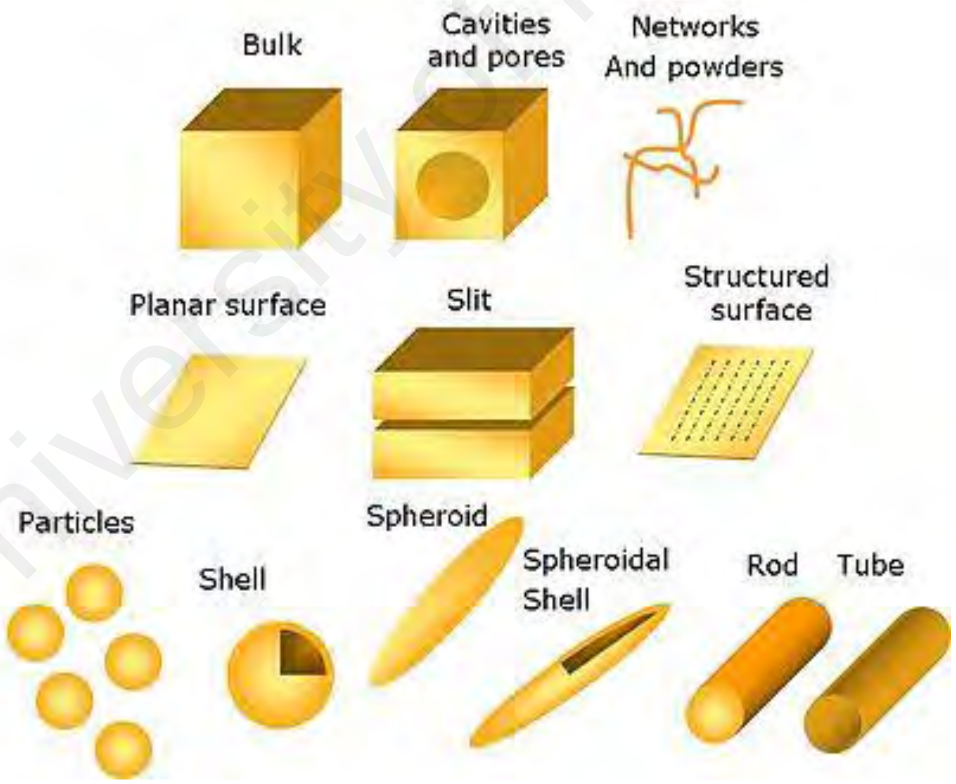

**Figure 2.2:** Typical nanostructure geometries (adapted from Wikibooks, 2013).

Nanostructure materials can be categorized as 0D (zero-dimensional), 1D, 2D and 3D (Tiwari et al., 2012). Zero- dimensional nanostructure materials such as uniform particles arrays (quantum dots), heterogeneous particles arrays, core–shell quantum dots, onions, hollow spheres and nanolenses have been synthesized by several research groups (Kim et al., 2010; Zhang & Wang, 2009). One dimensional (1D) , such as nanowires, nanorods, nanotubes, nanobelts, and nanoribbons have stimulated an increasing interest due to their importance in research and developments and have a wide range of potential applications.

2D nanostructures have two dimensions outside of the nanometric size range. In recent years, a synthesis of 2D nanostructures has become a focal area in materials research, owing to their many low dimensional characteristics different from the bulk properties. 2D nanostructure with certain geometries exhibit unique shape-dependent characteristics and subsequent utilization as building blocks for the key components of nanodevices (Tiwari et al., 2012) in sensors, photocatalysts, nanocontainers, nanoreactors, and templates for 2D structures of other materials. Examples of 2D nanostructure are branched structures, nanoprisms, nanoplates, nanosheets, nanowalls, and nanodisks.

It is well known that the behaviors of nanostructure are strongly depending on the sizes, shapes, dimensionality and morphologies, which are thus the key factors to their critical performance and applications. Therefore it is of great interest to synthesize 3D nanostructure with a controlled structure and morphology. Nanoballs (dendritic structures), nanocoils, nanocones, nanopillers and nanoflowers are the examples of 3D nanostructures.

## 2.4 Surface plasmon resonance (SPR)

There are three major physical properties of nanoparticles, and all are interrelated; first, they are highly mobile in the free-state. Second, they have enormous specific surface areas and third, they may exhibit what are known as quantum effects. Plasmonic nanoparticles are metal nanoparticles – including gold, silver, and platinum – that are highly efficient at absorbing and scattering light (Jain et al., 2007). By changing the size, shape, and surface coating, the optical properties of the nanoparticles can be tuned from the ultraviolet (Hulteen et al., 1999) to the visible to the near-infrared regions (Zakaria et al., 2014) of the electromagnetic (EM) spectrum. By shifting the absorption and scattering, the color of nanoparticle dispersions and films can also be tuned: for example, solutions of spherical gold nanoparticles are ruby red in color due to the strong scattering and absorption in the green region of the spectrum, while solutions of silver nanoparticles are yellow due to the plasmon resonance in the blue region of the spectrum (red and green light is unaffected).

The reason for the unique spectral response of silver and gold nanoparticles is that specific wavelengths of light can drive the conduction electrons in the metal to collectively oscillate, a phenomenon known as a surface plasmon resonance (SPR). When these resonances are excited, absorption and scattering intensities can be up to 40 times higher than identically sized particles that are not plasmonic. The brightness and tunability of plasmonic nanoparticle optical properties make them highly useful in numerous applications such as molecular detection (sensors) (Anker et al., 2008; Cubukcu et al., 2009), solar energy materials (Catchpole & Polman, 2008; Morfa et al., 2008), and cancer detection (Anker et al., 2008; Law et al., 2011; Skrabalak et al., 2007) and treatment.

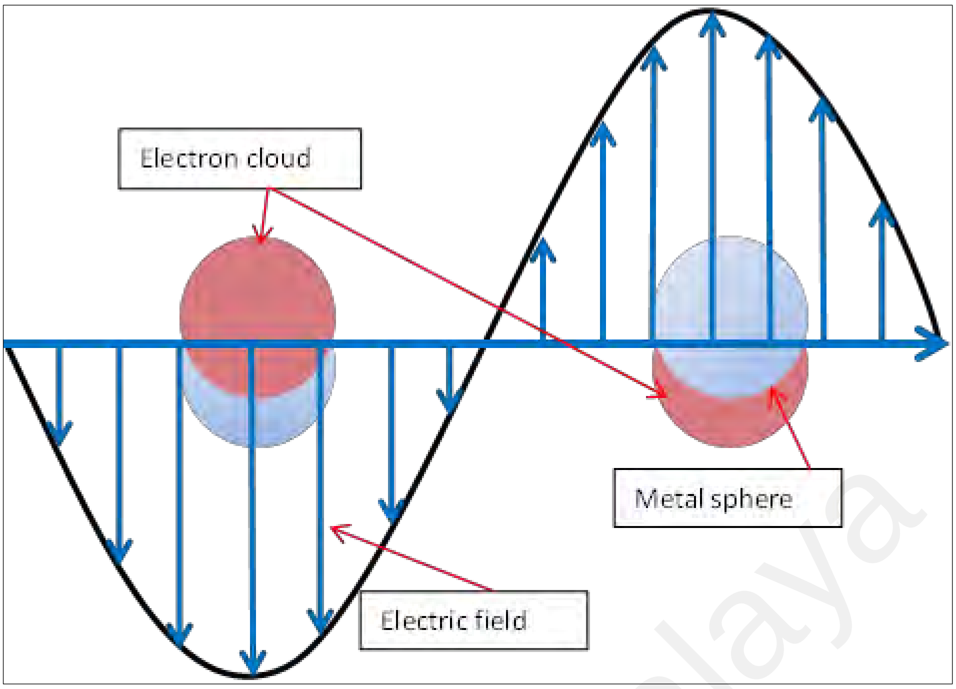

**Figure 2.3:** Schematic of surface plasmonic resonance. The free conduction electrons in the metal nanoparticle are driven into oscillation due to strong coupling with incident light (Kochuveedu & Kim, 2014).

Noble metal nanoparticles support surface plasmons (oscillations of the conduction electrons at the nanoparticle surface) that result in extraordinary optical properties that are not exhibited by any other class of material. The basis for the effect is the plasmon resonance of the free electrons in the metal nanoparticle, which can be understood by studying the polarizability (the ease with which charges, such as the conduction electrons on the metal nanoparticle surface, undergo charge distribution and form partial dipoles). For a spherical nanoparticle, the quasi-static polarizability of the nanoparticle is given by:

$$\alpha = 4\pi\varepsilon_0 r^3 \frac{\varepsilon_1(\omega)-\varepsilon_2}{\varepsilon_1(\omega)+2\varepsilon_2} \tag{2.1}$$

where $\varepsilon_1$ is the wavelength dependent dielectric function of the nanoparticle and $\varepsilon_2$ is the dielectric function of the medium which remains roughly constant regardless of wavelength. When the condition $\mathrm{Re}\{\varepsilon_1\} = -2\varepsilon_2$ is satisfied, the particle is driven into resonance resulting in a strong increase in the absorption and/or scattering at that wavelength.

The resonance condition depends on the wavelength dependent dielectric function of the nanoparticle as well as the dielectric function of the medium. Consequently, the nanoparticle optical properties are highly dependent on material composition, size, and the medium in which the particles are embedded (Jain et al., 2006). Both the shape and peak resonance wavelength of the nanoparticle plasmon resonance is influenced by the local refractive index. For examples, when particles are in water ($n$ = 1.33) the peak resonance of 80 nm Ag particles expected by Mie Theory is ~ 445 nm. In air ($n$ = 1.00) the peak wavelength of the plasmon resonance is predicted to be ~380 nm, a blue-shift of 65 nm.

The size effect on the width of SPR excitation in metal nanoparticles is well understood and results in the broadening of the SPR band for very small and for large nanoparticles (Anatoliy & Uwe, 2003). The size confinement of the conduction electrons in metal nanoparticles broadens the SPR band (Anatoliy & Uwe, 2003; Vollmer, 1995). The increase of the bandwidth with decrease of the nanoparticle size is caused by the scattering of conduction electrons on the surface of a nanoparticle. When the nanoparticle size increases, the SPR band broadens again due to the radiation damping (Dahmen et al., 2007; Yeshchenko, 2009). The width of the SPR is a very important factor determining, for example, the local field enhancement due to the SPR excitation, which is used in surface enhanced spectroscopy. Meanwhile, the size dependence of the SPR energy is somewhat uncertain (Vollmer, 1995). Though the classical electrodynamics theory, such as the Mie theory, predicts a blue shift for the SPR, when the nanoparticle size decreases, some experiments revealed different shifts of the SPR frequency. There are reports on both blue shift and red shift of the SPR frequency, as the size of nanoparticles decreases (Kreibig, 1986; Vollmer, 1995).

## 2.5 Organic semiconductors

Organic electronics attracted academician and industrial researchers due to promising applications such as OLED, OFET and Organic Photovoltaic Cell (OPVC). Conjugated $\pi$-electron system is used in these organic electronic devices (Facchetti, 2010). These materials are mainly constructed of hydrogen and carbon atoms but often contain other elements like nitrogen, oxygen or sulfur and even metals like aluminum, platinum or iridium. The lowest electronic excitation is a $\pi$-$\pi^*$ -transition between the highest occupied molecular orbital (HOMO) and the lowest unoccupied molecular orbital (LUMO) (Brütting, 2006).

The excited state is a coulombically bound electron-hole pair and is termed an exciton, i.e. a neutral electronic state with an excitation energy which is smaller than the energy required for the formation of a free electron-hole pair (Schwoerer & Wolf, 2007). The exciton binding energy is typically around 0.5 to 1 eV. Concerning charge transport, the carriers must be thermally activated in order to hop from molecule to molecule and the process of electrical conduction is referred to as hopping conduction (Schwoerer & Wolf, 2007). Due to the required thermal activation, the mobility in disordered molecular solids increases with rising temperature.

## 2.6 Organic Light Emitting Diode (OLED)

In this section, the basic progress of light emission through electrical excitation in an OLED will be discussed. In general, this effect is called electroluminescence (EL), whereas luminescence under excitation with light is termed photoluminescence (PL). From a historical point of view, the phenomenon of electroluminescence in organic light-emitting diodes (OLEDs) solids has been known for almost 50 years. Pope et al. as well as Helfrich and Schneider discovered and investigated the electroluminescence of anthracene single crystals between two electrodes (Helfrich & Schneider, 1965; Pope et al.,, 1963). They used highly-purified crystal platelets with a thickness between 10 µm and 5 mm, hence a high voltage of several hundred to more than thousand volts was required in order to create electroluminescence from the thick crystals.

In 1970, Williams and Schadt used laterally-structured electrodes to define the area of emission (Williams & Schadt, 1970). In addition, they encapsulated their device in order to protect it against air, which is basically still used nowdays. The major innovation occurred in 1987 when Tang and VanSlyke published their results about "Organic electroluminescent diodes" (Tang & VanSlyke, 1987) . They were the first to build a heterostructure OLED using low molecular weight evaporated organic thin films with a thickness of around 100 nm. This approach reduced the required voltage significantly, and an external quantum efficiency of 1 photon per 100 injected electrons was obtained. Three years later, the first OLED using polymers deposited from solution by spin coating was produced (Burroughes et al., 1990). These results were the beginning of a worldwide research and development in the field of OLEDs, both based on small molecules and polymers.

### 2.6.1 OLED device structure and operation

A simplified OLED structure consists of cathode, ETL, recombination layer/emission layer, hole transport layer (HTL) and anode. When a driving voltage of 5 to 10 V is applied across the two metallic electrodes, electrons are injected from the cathode (low work function), into electron transport layer (Farzinpour et al., 2012) where the electrons jump via the LUMOs of neighboring molecules towards the anode. Similarly, holes are injected from the anode and transport in HTL. In this way, electrons and holes can recombine and form excitons in the recombination layer (Figure 2.6).

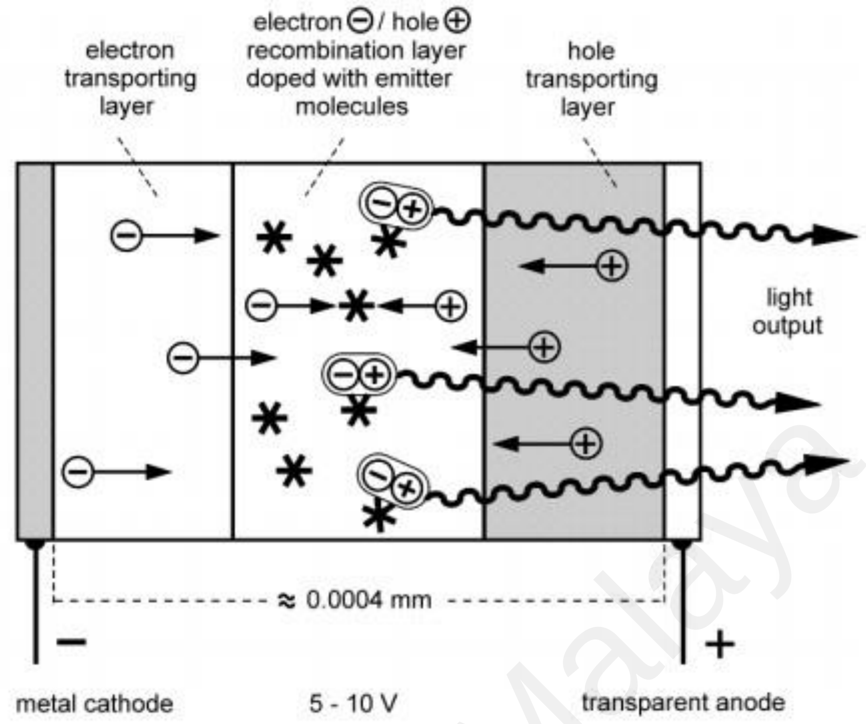

**Figure 2.4:** Schematic diagram of OLED's structure and working principle (adapted from Yersin, 2004).

Usually the anode of an OLED is a transparent metal oxide layer with good conductivity, which allows the light generated in the recombination layer to be emitted out. Indium tin oxide (ITO) is a widely used anode material in OLEDs, consisting of $SnO_2$ (10-20 %) and $In_2O_3$ (90-80 %). Different methods have been developed to deposit ITO on glass substrates such as thermal evaporation, sputter deposition, and so on. ITO exhibits a relatively high work function, which is suitable for hole injection into the HOMO of the HTL material. The electron and hole mobility in organic materials are in orders of magnitude smaller than those in crystalline inorganic semiconductors owing to the localized nature of the electronic states in amorphous organic materials. This offers enough time for electron/hole recombination, making a highly efficient EL possible under a low driving voltage.

A simple OLED structure is not able to achieve highly efficient EL. Power efficiency losses can originate from many reasons, such as poor alignment of the electrodes work functions relative to the HOMO/LUMO of the adjacent layers, unbalanced electron and hole mobility, a low cross-section for electron-hole recombination, low light outcoupling efficiency and so on.

An OLED can be fabricated in various ways depending on the material features. Generally speaking, vacuum thermal deposition and wet-coating are two main techniques for OLED processing. Thermal evaporation is applied to small molecules and metals which are sublimated by the Joule effect and evaporated in a vacuum of ~ $10^{-6}$ Torr or higher. One of the most prominent advantages of vacuum thermal deposition is that it enables the fabrication of multilayer devices in which the thickness of each layer can be controlled precisely. So far the vacuum thermal deposition techniques for OLEDs fabrication are successfully transplanted from the sophisticated semiconductor industry.

### 2.6.2 SPR effect in OLED

OLEDs have received great attention as potential next-generation displays due to their low power consumption, excellent color range, fast response time, and especially their flexibility (Kim et al., 2013). Although almost 100 % internal quantum efficiency of OLEDs has been achieved by using phosphorescent emitters and optimizing device structures (Adachi, 2001), the external quantum efficiency (EQE) of OLEDs is still limited due to poor light extraction (Kim et al., 2013; Kim et al., 2014; Madigan et al., 2000). The key challenge is to improve the extraction of light trapped between layers and the energy transfer between donor and acceptor molecules in emissive layers.

One useful strategy for light trapping and emitting in OLEDs is to exploit the surface plasmon resonance (SPR) effect of metal nanostructures. Surface plasmons are collective oscillations of free electrons at the interface between the metal and dielectric (Kulkarni et al., 2010; Linic et al., 2011). The SPR effect, which is induced by an electric field at specific incident wavelength, leads to intense surface plasmon absorption bands and strong light scattering with concurrent strengthening of local electromagnetic fields (Atwater & Polman, 2010; Kumar et al., 2012).

By exploiting either localized surface plasmons (LSPs) excited in metal nanoparticles (NPs) or surface plasmon polaritons (SPPs) propagating at the interface between metal and semiconductor, the light can be efficiently concentrated into a thin active layer, thereby maximizing the light absorption. In particular, metal NPs function as effective subwavelength antennas and scattering elements to store the incident energy in LSP modes and to increase the optical path length of the incident light within the active layer, leading to photogeneration of charge-carriers (Figure 2.5) (Atwater & Polman, 2010).

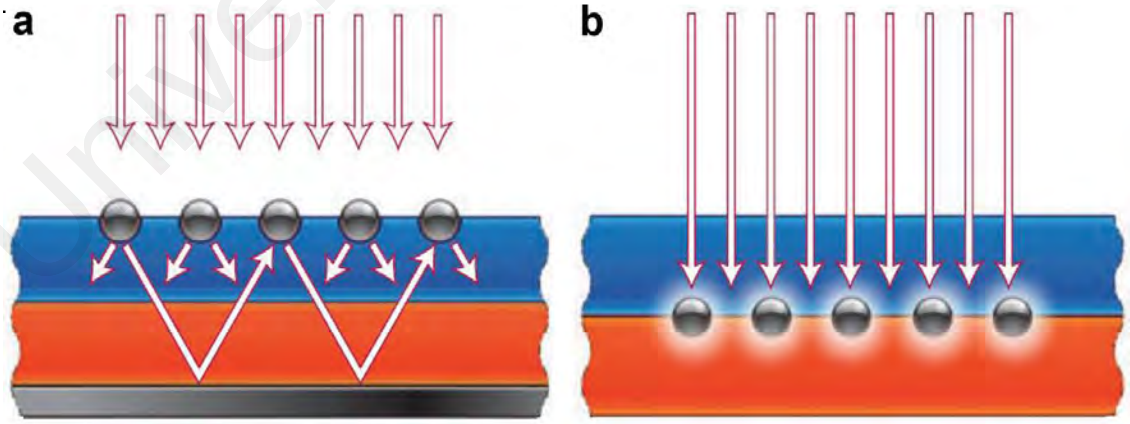

**Figure 2.5:** Plasmonic light-trapping mechanism of metal NPs: (a) light trapping by scattering from metal NPs at the surface of the device and (b) light trapping by the excitation of SPs in metal NPs embedded in semiconductor (adapted from Atwater & Polman, 2010).

Among various metal NPs, Ag NPs have exhibited the most effective light trapping potential due to their strong light scattering and surface plasmon strength (Gaspar et al., 2013). In addition, SPR absorption spectra of silver nanoparticles (Ag NPs) can be controlled from 300 (ultraviolet (UV)) to 1200 nm (near-infrared (NIR)) (Chen et al., 2012; Rycenga et al., 2011). The ability of metal NPs for SPR effect depends on its dielectric function $\varepsilon$ including a real part $\varepsilon_r$ and an imaginary part $\varepsilon_i$, both of which vary with excitation wavelength $\lambda$. (Rycenga et al., 2011) The SPR effect of metal NPs with spherical structure can be described using the extinction (absorption + scattering) cross-section based on Mie theory (Mulvaney, 1996),

$$C_{ext} = \frac{24\pi^2 R^3 \varepsilon_m^{\frac{3}{2}}}{\lambda}\left[\frac{\varepsilon_i}{(\varepsilon_r+2\varepsilon_m)^2+\varepsilon_i{}^2}\right] \tag{2.2}$$

where $C_{ext}$ is the extinction cross-section, $R$ is the NP radius, and $\varepsilon_m$ is the relative dielectric constant of the matrix surrounding the metal NPs. This equation implies that dielectric properties have strong effect on the interaction between light and metal NPs.

In addition, the SP strength (or damping) of metal NPs can be expressed using the quality factor (*QF*) (Ru & Etchegoin, 2009),

$$QF = \frac{w(\frac{d\varepsilon_r}{dw})}{2(\varepsilon_i)^2} \tag{2.3}$$

SP strength is proportional to QF. Specifically, high QF indicates strong plasmons and low QF means weak SP with a small $C_{ext}$. Ag has higher QF than do other metals over the spectrum from 300 to 1200 nm. Interband transitions (IBTs), which are excitations of electrons from the conduction band to higher energy levels, are key factor for the SP strength. (Perner et al., 1997) In Ag, these transitions occur at much higher energies than the SPR, whereas these transitions limit their SPR excitation to wavelength >500 nm for Au and >600 nm for Cu. (Heo et al., 2011; Wang et al., 2005) Taking into account, these factors and others including plasmonic ability, material cost, and chemical stability, Ag is the most economical and effective candidate for plasmonic applications.

Other group elsewhere has used different technique and parameter but with the same aim; to achieve high efficiency in their OLED by incorporating nanoparticles. Kumar et al., 2012 enhanced blue OLED by using silver nanoclusters (SNCs) deposited using thermal evaporation technique and achieved the efficiency two times higher than reference OLED without SNCs (Kumar, 2012). Internal quantum efficiency was calculated to be 24 % for SP enhanced OLED owing to 96 % fluorescence efficiency. Meerheim et al., 2008 achieved high efficiency of green, red and blue OLED by incorporating silver layer on ITO. They reach 81 lm/W for red, 101 lm/W for green, and 4.0 lm/W for blue OLED (Meerheim et al., 2008). Those efficiencies are improved by up to a factor of 2.3 compared to standard ITO device which attributed to microcavity amplification between the cathode and the silver layer.

# CHAPTER 3: EXPERIMENTAL METHOD

## 3.1 Introduction

This chapter will briefly describe the experimental details employed in the process of producing OLED, starting from cleaning of the ITO substrates, then the production of the nanoparticles with the material characterisations and the device fabrications.

## 3.2 Preparation for pre-patterned ITO substrates

Properties of pre-patterned ITO substrate are shown in Table 3.1. The loaded substrate on the rack was submerged in a beaker with hot sodium hydroxide (NaOH) 10% solution to remove dust and provide hydrophilic surface. The beaker was placed in sonicator and sonicate for 10 minutes using hot bath. Then the substrates were rinsed thoroughly with deionized water. The substrates rack was put in a beaker of acetone and sonicated again for 15 minutes to remove any organic residues. The sonicating process repeated using IPA and deionized water. The substrates were immersed in deionized water to avoid contaminations until it is ready to blow dry using nitrogen gas.

**Table 3.1:** Patterned ITO substrates properties.

| | |
|---|---|
| Substrate dimensions | 20 mm × 15 mm |
| Pixel dimensions (with cathode) | 3 mm × 1.5 mm (4.5 $mm^2$) |
| Glass type | Polished Soda Lime, Float |
| Glass thickness | 0.7 mm |
| Substrate coating | Fully Oxidized ITO |
| ITO thickness | 100 nm |
| ITO resistance | 20 Ohm/square |

### 3.3 Deposition of silver thin film

Edward 306 electron beam evaporator was used to deposit silver (Ag) thin film on the clean pre-patterned ITO. The thickness was varied by manipulating the deposition time and keeps the pressure of the chamber constant at 2 x $10^{-5}$ mbar with 25 mA current and external voltage of 4 kV. Film thicknesses were measured using a P-6 profiler-meter (KLA-Tencor). All samples went through annealing treatment in furnace at 250 $^{o}$C for 2 hours. Silver nanoparticles were confirm exist on the substrate after observing using JEOL Field Emission Scanning Electron Microscope (FESEM).

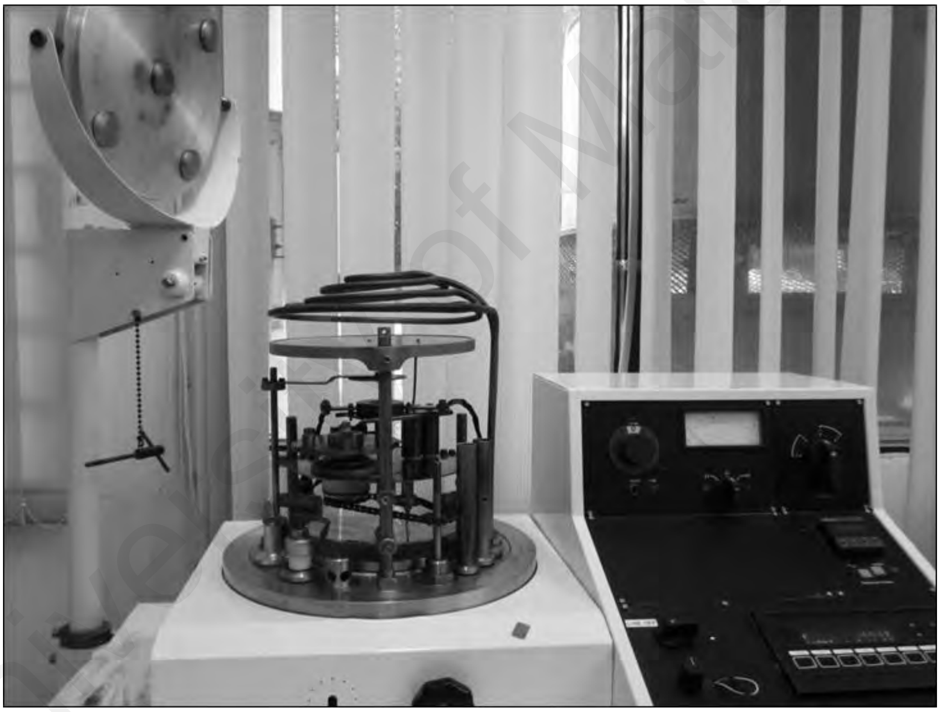

**Figure 3.1:** The AUTO 306 Vacuum Coater.

The surface morphology of the films was investigated via Atomic Force Microscopy (AFM, NT-MDT NTEGRA-Prima) and UV-Vis Spectrometer was used to measure the light absorption (SPR) by the nanoparticle related to the thickness of Ag thin film.

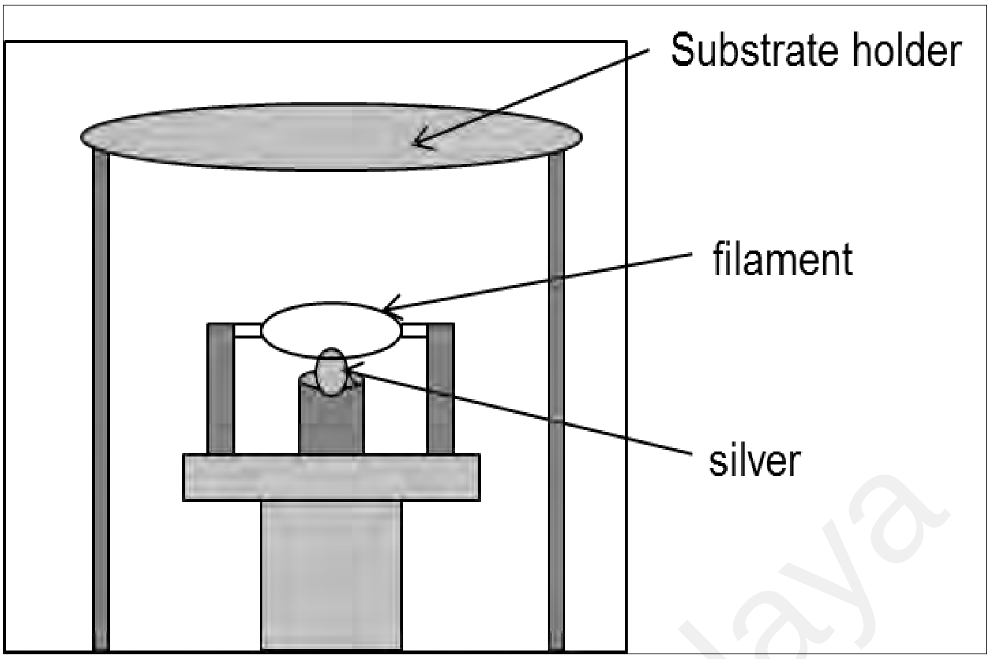

**Figure 3.2:** Schematic diagram of the e-beam evaporator.

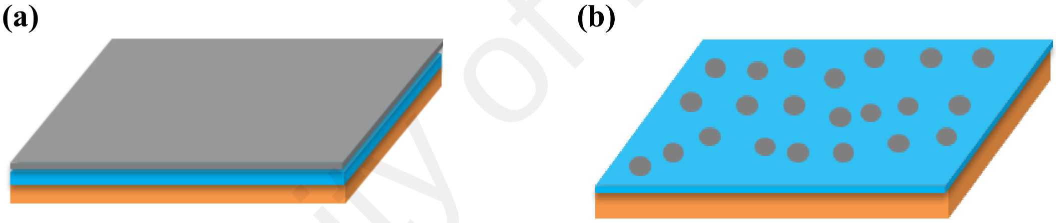

**Figure 3.3:** Ilustration of dewetting process (a) layer of silver thin film on top of ITO substrate and (b) assembled silver nanoparticle after thermal annealing.

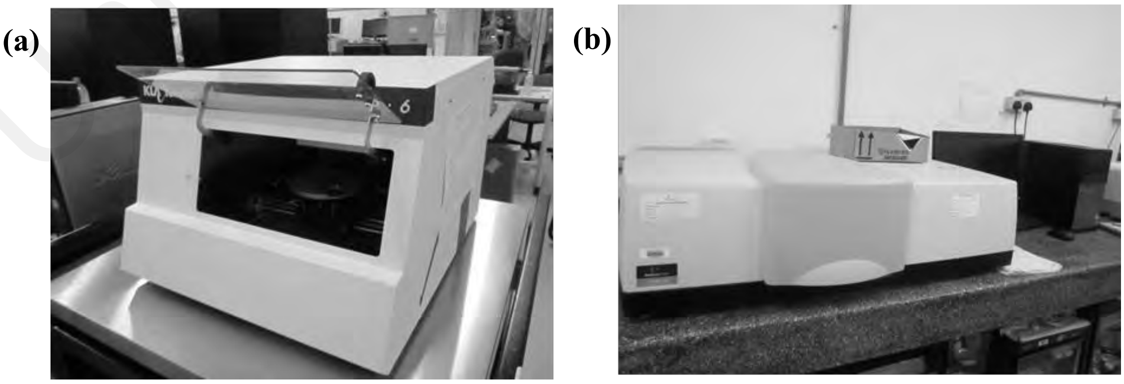

**Figure 3.4:** (a) P-6 TENCOR Profilometer and (b) UV-Vis Spectrometer.

## 3.4 Organic Light Emitting Diode (OLED) device fabrication

All materials were purchased and used as received without further purification. PVK (average $M_w$ = 1,100,000 g/mol) and Ag NPs were purchased from Sigma-Aldrich while PBD were purchased from Lumtech. Tris[2-(p -tolyl)pyridine]iridium(Morfa et al.) ($Ir(mppy)_3$, and Iridium (Morfa et al., 2008) bis(2-(2'-benzo-thienyl)pyridinatoN,C3') (acetyl-acetonate) ($Ir(piq)_2acac$) which are green and red emitter respectively was obtained from American Dye Inc. The device structure for control device consists of ITO (100 nm) / PEDOT:PSS (Al 4083) (40 nm) / EML (80 nm)) / LiF (1 nm) / Al (100 nm). While for the device with Ag NPs, 20 nm of Ag NPs was deposited on top of ITO prior PEDOT:PSS spin-coating.

PEDOT:PSS serves as a hole injecting layer while EML is the emissive layer containing the hosts and the emitter. High quality PEDOT: PSS film is critical for effective device performance and is often the most difficult part of device fabrication. PEDOT: PSS requires a pristine and hydrophilic surface in order to coat properly, which should have been achieved with the cleaning routine above in Section 3.2. LiF is the electron injecting layer while ITO and Al are the anode and cathode respectively. The EML layer for the device is PVK: PBD: dye ($Ir(mppy)_3$ for green and $Ir(piq)_2acac$ for red OLED) with a blending ratio of 70:24:6. Layer of PEDOT: PSS was spin-coated on top of the substrates at 1500 rpm for 30 seconds to yield a film thickness of 40 nm. After spinning has completed, visual inspection was done for the PEDOT: PSS films for defects. PEDOT: PSS was wiped off the cathode with a cotton bud soaked in DI water and placed directly on a hotplate inside glove box with $N_2$ environment for 10 minutes at 150 $^{o}$C to remove residual water.

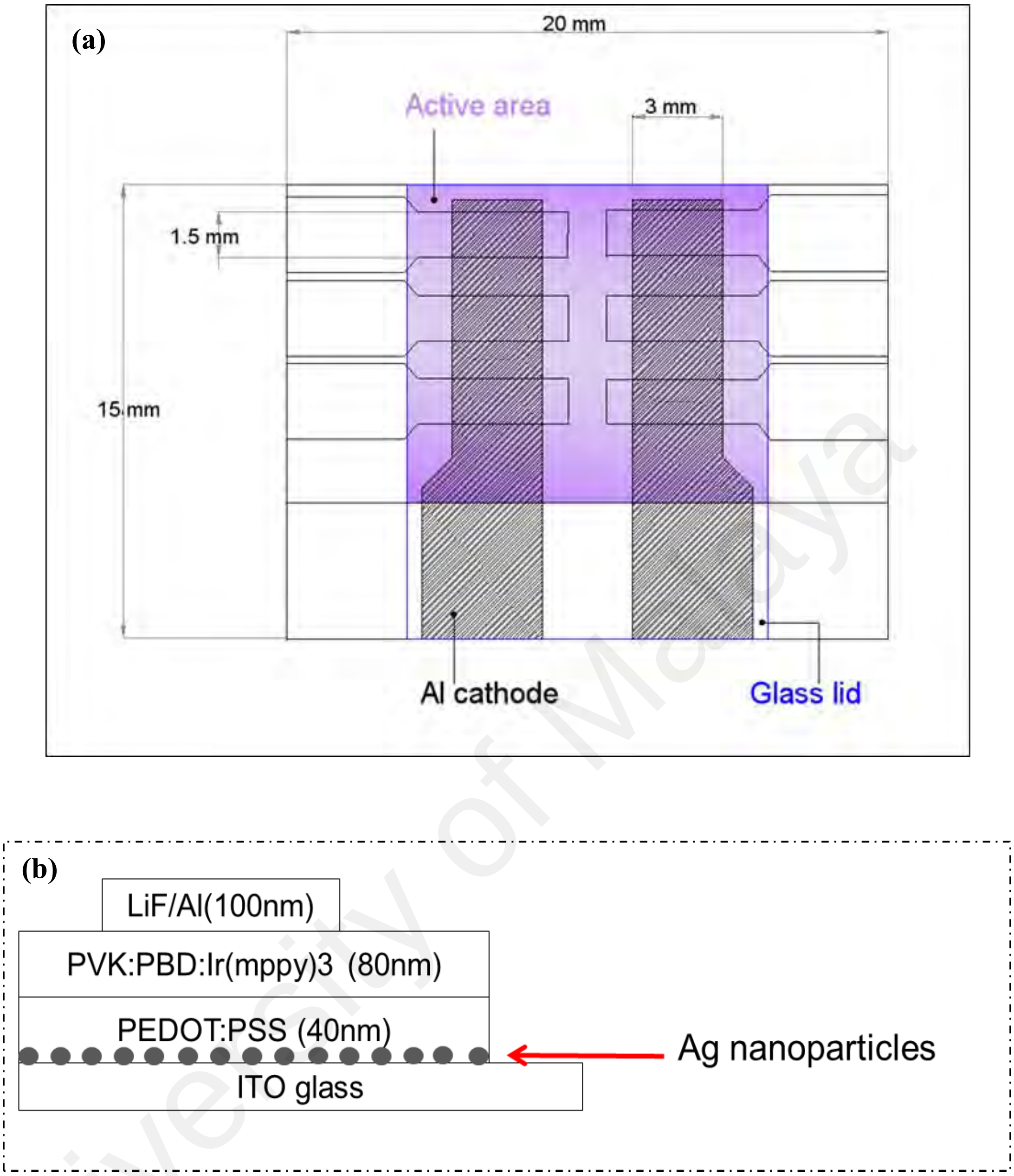

**Figure 3.5:** (a) Schematic of patterned ITO substrate and Al cathode on top of it for control device and (b) schematic diagram of plasmonic device structure.

The EML dissolved in chlorobenzene was spin coated on top of PEDOT: PSS and then baked at 80 °C for 30 minutes. Next, 1 nm of CsF and 100 nm of Al were vacuum deposited sequentially at a base pressure of 2.5 x $10^{-4}$ mbar without breaking the vacuum. All the devices were encapsulated using UV curable epoxy and glass lid. Encapsulating the devices as shown in Figure 3.6 protects them against degradation by oxygen and moisture once removed from the glove box.

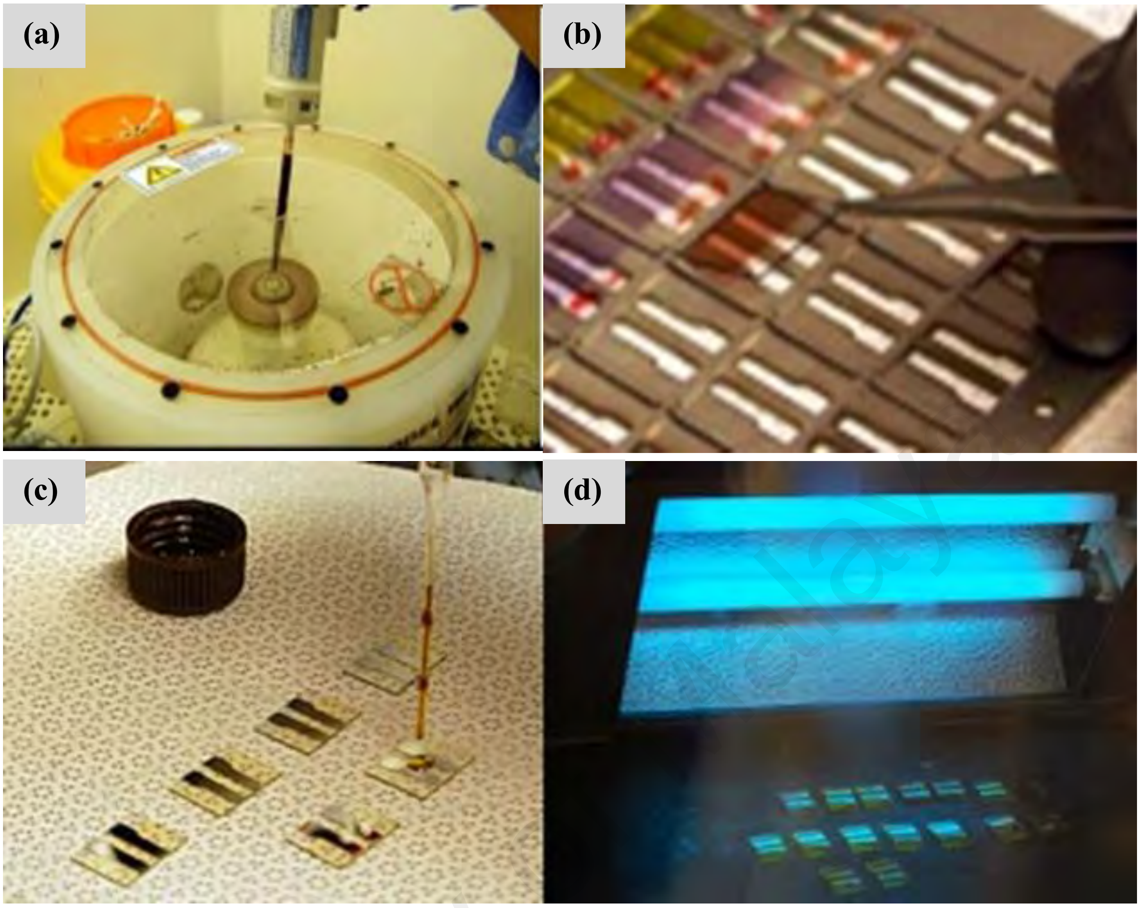

**Figure 3.6:** Fabrication processes (a) PEDOT: PSS spin coating, (b) preparation for Al (cathode) deposition, (c) epoxy dropped-on and (d) UV encapsulation.

## 3.5 IVL setup for electrical measurement

The device current-brightness-voltage ($I$-$V$-$L$) characteristics were measured using Konica Minolta Cs-200 integrated with Keithley 276 source meter. The generated photocurrent was converted into a voltage by current-to-voltage converter with an analog devices amplifier and a resistor. In such a converter, the output voltage, $V$ is related to the photocurrent, $I$ according to Ohm’s Law:

$$V = IR \tag{3.1}$$

The output voltage from the light power measurement was read by a computer using digital acquisition board. Light and current measurements were implemented in a LabView program for simultaneous testing. The testing was done immediately after the encapsulation.

## 3.6 FESEM machine principle

Field Effect Scanning Electron Microscope (FESEM) is used to observe small structure on the surface of cell or materials. Electrons from a field emission source are accelerated in high electrical field. Operated in high vacuum, these primary electrons are focused and deflected by electronic lenses to produce narrow scan beam that bombards the object and emit secondary electrons from each spots on the object (Figure 3.7). The secondary electrons, which are attracted by the Corona, strike the scintillator (fluorescing mirror) that produces photons. The location and intensity of illumination of the mirror vary depending on the properties of the secondary electrons.

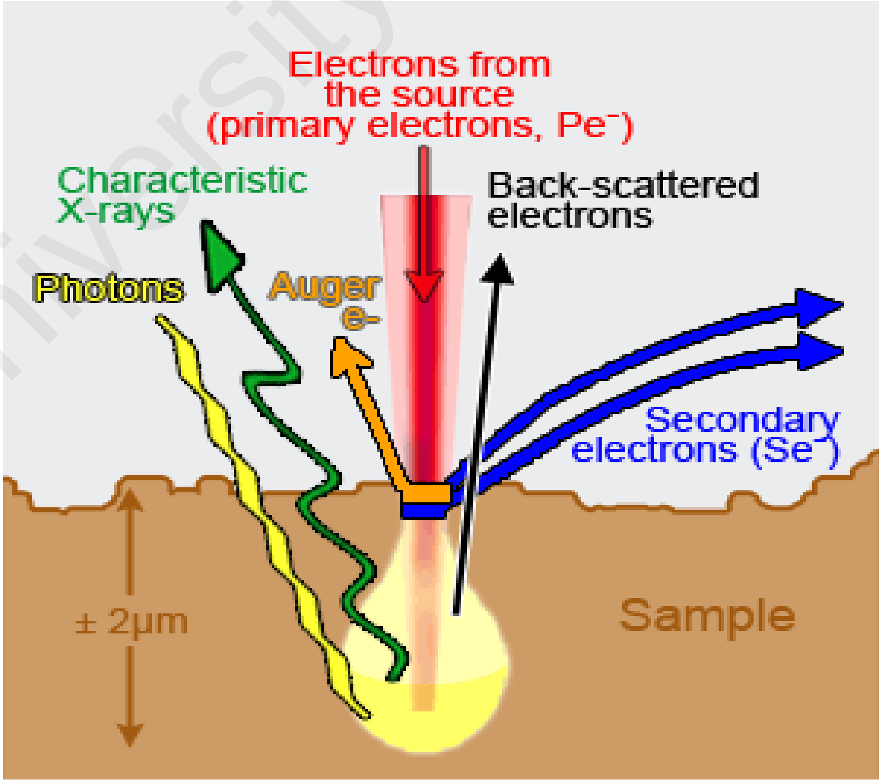

**Figure 3.7:** Primary electrons strikes sample and yield different type of particle (Nijmegen, 2014).

The signal produced by the scintillator is amplified and transduced to a video signal that is fed to a cathode ray tube in synchrony with the scan movement of the electron beam. The contrast in the 'real time' image that appears on the screen reflects the structure on the surface of the object.

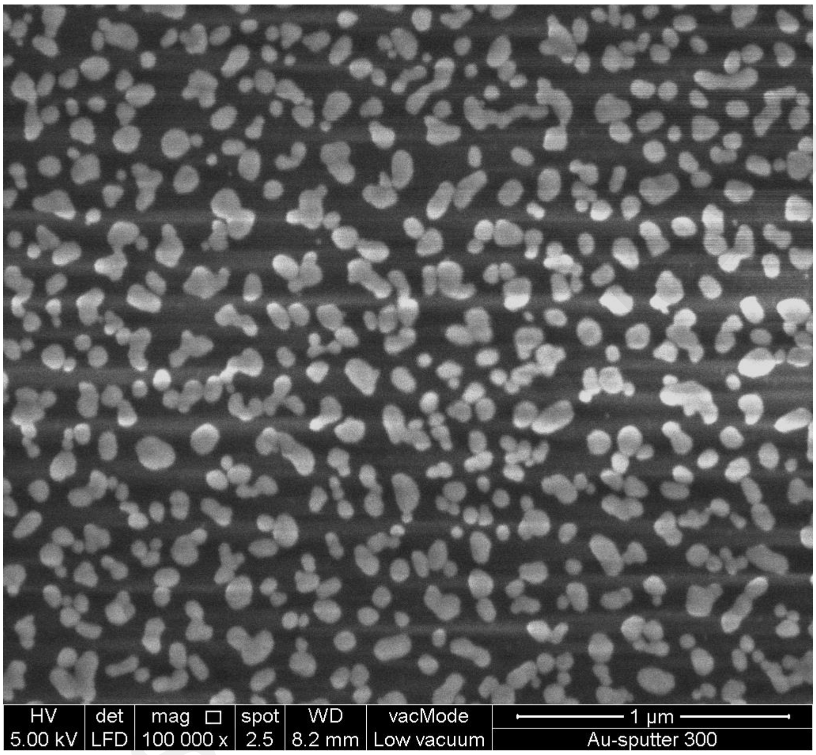

**Figure 3.8:** FESEM image of gold nanoparticles.

The more secondary electrons reach the scintillator, the brighter the signal is at that point. This luminescence signal is further amplified by a photomultiplier tube and transduced to a video signal that is fed to a cathode ray tube in synchrony with the scan movement of the electron beam. The analog image is converted to a monochromatic (grey shades) computer image that can be further digitally processed as shown in Figure 3.8.

### 3.7 AFM machine and principle

Atomic force microscopy (AFM) is a type of Scanning Probe Microscopy, is used to imaging surfaces with nanometer resolution, and to determine surface roughness, probe local changes in friction, measure surface forces, and assess changes in local elasticity over a sample surface. An ultra-fine tip or needle attached to the cantilever beam is scanned across the surface of the sample to measure surface morphology and properties to construct a 3-D image of the surface. Its resolution is from few microns to below 10 Angstroms.

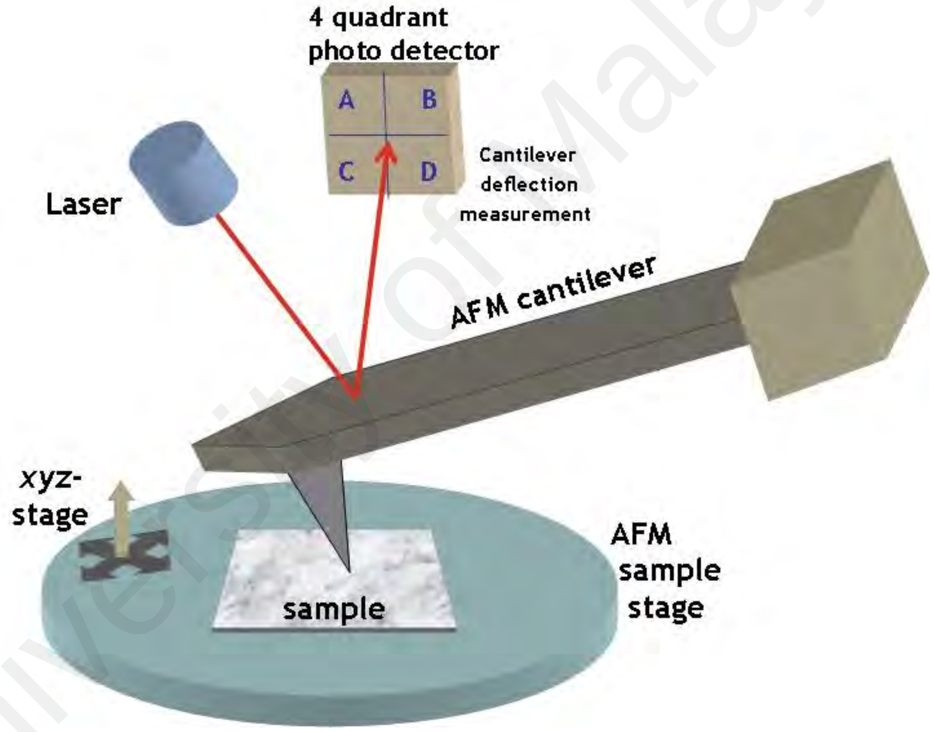

**Figure 3.9:** Diagram representing AFM working principle (source: http://web.stevens.edu/nue/about.html).

The microscope typically uses a laser beam deflection system to image the surface topography of a sample. AFM operates by using a tip attached at the free end of a cantilever, to probe the sample's surface. The tip may come into direct or close contact with the surface, so that they may both interact with each other through attractive or repulsive forces (e.g. electrostatic, Wan der Waals etc.), depending on the proximity of the tip to the surface. These forces *(F)* are measured by Hook's Law:

$$F = -kz \tag{3.2}$$

where $k$ is the cantilever stiffness and $z$ the distance of the cantilever deflection measured through the laser beam deflection system.

The laser beam is reflected by the upper part of the cantilever. A photodetector measures the deflection of the laser beam and the data is converted into a topography image of the probed surface. Other measurements include the surface roughness, distance, and peak-to-valley measurements. These different types of analysis can be acquired through the different scanning modes that the AFM can operate with.

## 3.8 Profilometer principle

P-6 Tencor profilometer is used to measure step height, roughness, and waviness on samples surface. Roughness can be measured over short distances and this system uses stylus-based scanning to achieve high resolution and can correlate local submicron features with surface measurements. It works by monitoring the height of a stylus as it drags across a step in the film (Figure 3.10). ‘Scan recipe’ was set up to specify the scan parameters such as length, speed, sampling rate, and the force to be applied on the sample surface. A slow scan speed will drastically affect throughput, whereas a fast scan speed may cause the stylus to bounce and lose contact with the surface. The primary advantage of stylus profilometry is that it can be used on all solid films, including opaque materials such as thick metal films.

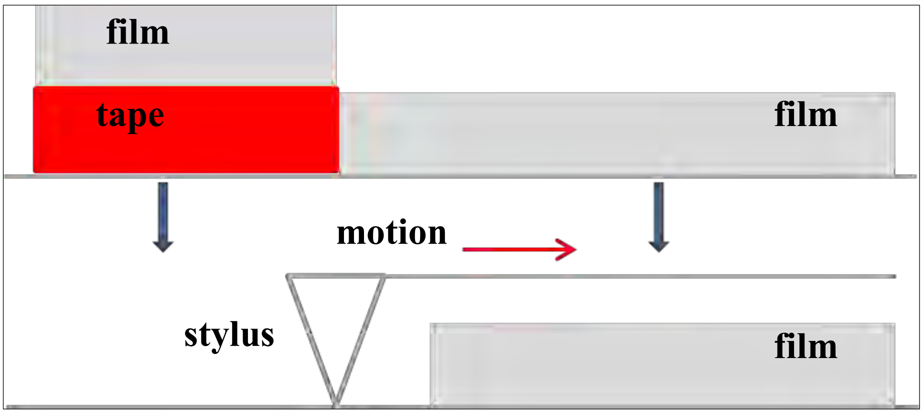

**Figure 3.10:** Stylus profilometer measurement on a film.

## 3.9 Optical characteristic measurement

### 3.9.1 UV-Vis setup and principle

Radiation is a form of energy and may be considered in terms of a wave motion where the wavelength, $\lambda$, is the distance between two successive peaks. The frequency, *v*, is the number of peaks passing a given point per second. These terms are related so that:

$$c = v\lambda \tag{3.3}$$

where *c* is the velocity of light in a vacuum.

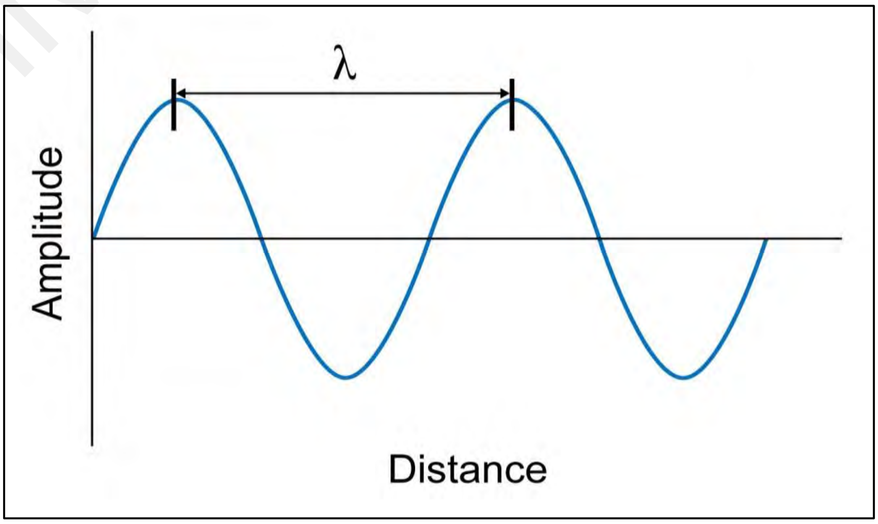

**Figure 3.11:** The wavelength, λ of electromagnetic radiation.

The full electromagnetic radiation spectrum is continuous and each region merges slowly into the next. For spectroscopy purposes, we choose to characterize light in the ultraviolet and visible regions in terms of wavelength expressed in nanometers.

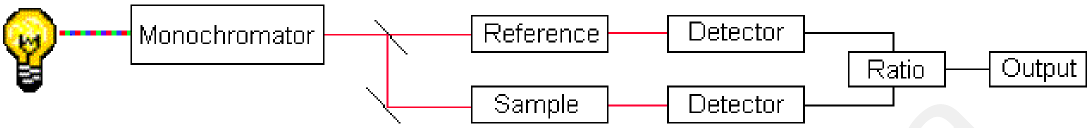

**Figure 3.12:** Schematic diagram of UV-Vis spectrometer working principle.

A beam of light from a visible and ultra violet light (Figure 3.12) separated into its component wavelengths by a prism or diffraction grating. Each monochromatic (single wavelength) beam in turn is split into two equal intensity beams by a half-mirrored device. One beam, the sample beam, passes through the Ag deposited ITO. The other beam, the reference, passes through a reference sample which is plain ITO. The intensities of these light beams are then measured by electronic detectors and compared. The intensity of the reference beam, which should have suffered little or no light absorption, is defined as $I_0$. The intensity of the sample beam is defined as $I$. Over a short period of time, the spectrometer automatically scans all the component wavelengths in the manner described. The ultraviolet (UV) region scanned is normally from 200 to 400 nm, and the visible portion is from 400 to 800 nm. Suppose the sample compound does not absorb light of a given wavelength, thus $I = I_0$.

However, if the sample compound absorbs light, then $I$ is less than $I_0$, and this difference may be plotted on a graph versus wavelength, as shown (Figure 3.13). Absorption may be presented as transmittance ($T = I/I_0$) or absorbance ($A = \log I_0/I$). If no absorption has occurred, $T = 1.0$ and $A = 0$. The wavelength of maximum absorbance is a characteristic value, designated as $\lambda_{max}$.

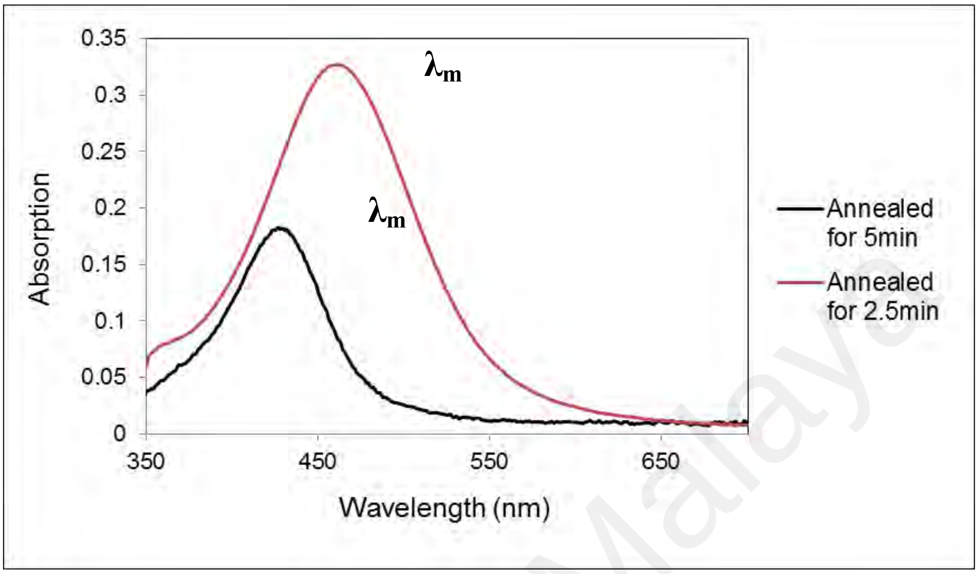

**Figure 3.13:** Absorption peak with $\lambda_{max}$.

### 3.9.2 Photoluminescence principle

The electronic states of most organic molecules can be divided into singlet states and triplet states where, singlet state is when all electrons in the molecule are spin-paired and triplet state is when one set of electron spins is unpaired (Figure 3.14).

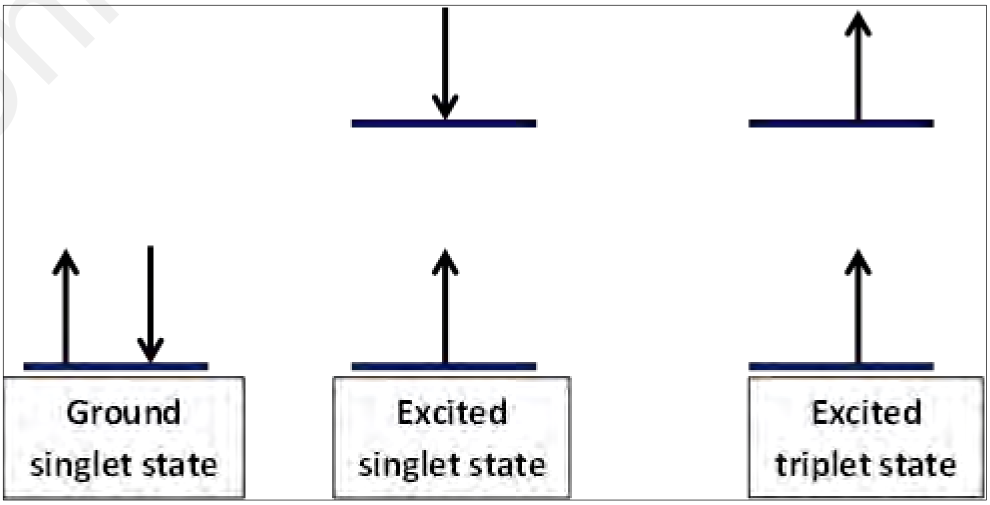

**Figure 3.14:** Electronic states of organic molecules.

Photoluminescence (PL) is when any form of matter absorbs photons (electromagnetic radiation). It occurs when an electron returns to the electronic ground state from an excited state and loses its excess energy as a photon. PL is divided into fluorescence and phosphorescence (Figure 3.15).

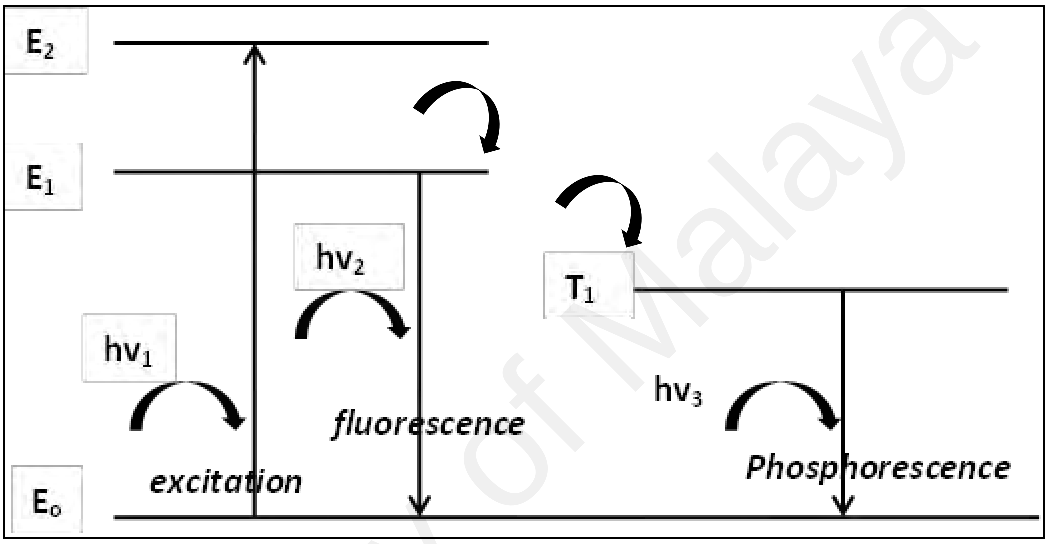

**Figure 3.15:** Fluorescence and phosphorescence level of electronic excited state.

### 3.9.2.1 Fluorescence

Absorption of UV radiation by a molecule excites it from a vibrational level in the electronic ground state to one of the many vibrational levels in the electronic excited state. This excited state is usually the first excited singlet state. A molecule in a high vibrational level of the excited state will quickly fall to the lowest vibrational level of this state by losing energy to other molecules through collision. The molecule will also partition the excess energy to other possible modes of vibration and rotation. Fluorescence occurs when the molecule returns to the electronic ground state, from the excited singlet state, by emission of a photon.

#### 3.9.2.2 Phosphorescence

A molecule in the excited triplet state may not always use intersystem crossing to return to the ground state. It could lose energy by emission of a photon. A triplet/singlet transition is much less probable than a singlet/singlet transition. The lifetime of the excited triplet state can be up to 10 seconds, in comparison with $10^{-5}$ s to $10^{-8}$ s average lifetime of an excited singlet state. Emission from triplet/singlet transitions can continue after initial irradiation.

## 3.10 SIMULATIONS SOFTWARE (FDTD)

FDTD used in this work are as introduction to the utility and functions in the software towards better simulation of the device in future works. Simulation's methodologies that need considerations are Source, Simulation Region, Mesh Refinement, and Monitor and Analysis. The simulation set up is also explained below.

### 3.10.1 Source

For devices that are periodic arrays like in our case, we often want to study the resonant transmission or reflection properties. Plane wave sources should always be used for periodic simulations. When using sources such as dipoles and Gaussian beams with periodic boundaries, the sources will also be copied across each unit cell in the periodic directions, which is unphysical. For sources at normal incidence, or for single frequency simulations with injection at normal incidence, the plane wave type should be set to "Bloch/Periodic".

### 3.10.2 Simulation region

When using the "Bloch/Periodic" plane wave type Figure 3.16, periodic boundaries should be used if the source is injected at normal incidence, and Bloch boundaries should be used when the source is injected at angled incidence in the directions where the structure is periodic. When using the "BFAST" plane wave type, the boundary conditions in periodic directions is automatically set to use the BFAST technique, so the boundary conditions in those directions do not need to be set. In the directions of periodicity, the simulation span must correspond to exactly 1 unit cell of the device.

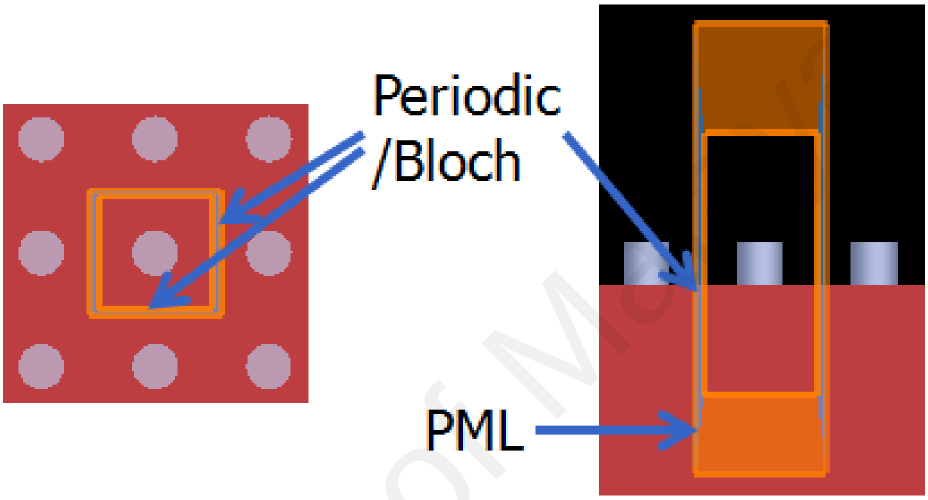

**Figure 3.16:** Periodic/ bloch plane wave (source: https://www.lumerical.com/).

Note that symmetry can still be used for periodic boundaries by setting the min/max settings to be the same. The settings in Figure 3.17 below correspond to a periodic simulation.

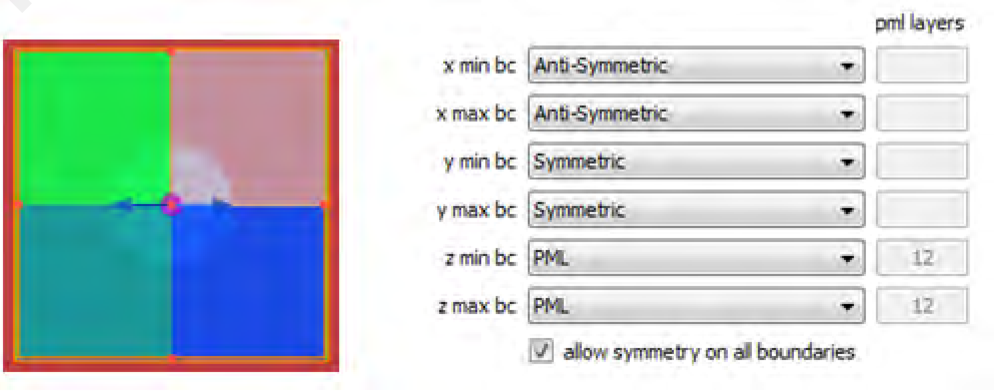

| | | pml layers |
|---|---|---|
| x min bc | Anti-Symmetric | |
| x max bc | Anti-Symmetric | |
| y min bc | Symmetric | |
| y max bc | Symmetric | |
| z min bc | PML | 12 |
| z max bc | PML | 12 |

☑ allow symmetry on all boundaries

**Figure 3.17:** Symmetric setting for periodic boundaries (source: https://www.lumerical.com/).

### 3.10.3 Mesh refinement

With the FDTD method, it is not possible to resolve interfaces to higher precision than the size of the mesh used. This is an important issue to consider for plasmonic simulations, since the results are often very sensitive to the size of the mesh near interfaces. The solution is to use mesh override regions to force a very small spatial mesh to more accurately resolve the locations of the metal interface. The disadvantage of this method is that it can greatly increase simulation times and memory requirements. Lumerical's conformal mesh technology allow us to obtain more accurate results for a given mesh size, so it is always worth considering this mesh refinement method over the traditional stair-casing method. Conformal variant 0 is the default setting. Note that with simulations that involve metal structures, the default conformal mesh reverts to stair-casing for all metal interfaces. In this case, we need to specify a variant of the default conformal mesh to take advantage of the conformal mesh technology if necessary. When using conformal mesh technology with metals, some convergence test need to be done to be sure that the conformal mesh technology is appropriate for our precise application.

### 3.10.4 Monitor

We are only interested in the total transmission/reflection of the device. This can be easily calculated by placing power monitors above and below the structure Figure 3.18, and then plotting the transmission in the Results View window. Note that power flowing towards the -x/-y/-z directions will carry a negative sign.

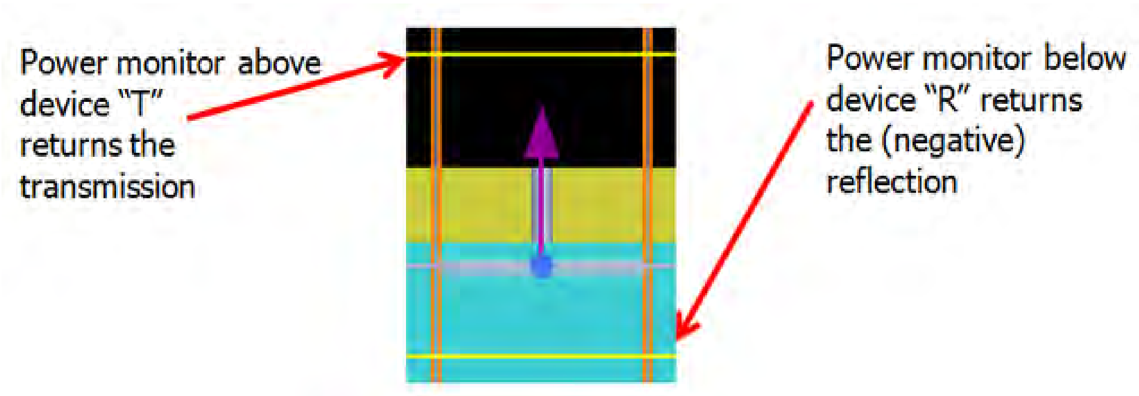

**Figure 3.18:** Location of 'power monitors' (source: https://www.lumerical.com/).

### 3.10.5 Simulation setup

We simulated an array of silver nanoparticles of radius 25 nm in a 20 nm, 30 nm, 35 nm, and 40 nm thick layer of silver. The silver layer uses the "Ag (Silver) - CRC" model included in the default material database. The plane wave source covers a wavelength range of 350 nm to 750 nm. A single unit cell of the array is modeled, and symmetric/anti-symmetric boundary conditions are used to further reduce the simulation volume by a factor of 4. (Please note that symmetric/anti-symmetric boundaries must be consistent with the source polarization) With an FDTD mesh accuracy of 2, and a 10 nm mesh override in the silver, the simulation runs in a few seconds on a single computer. Some convergence testing of the mesh size have been done for each simulation and typically mesh sizes of 5 nm or less was used for the final results.

# CHAPTER 4: TEMPERATURE AND THICKNESS OF SILVER NANOPARTICLES DEPENDANCE OF SPR: EXPERIMENTAL AND SIMULATIONS.

## 4.1 Introduction

Localized Surface Plasmon Resonance (LSPR) arises in metal NPs as a collective oscillation of the surface electrons when subjected to the electric field associated to the incident light (Atwater & Polman, 2010; Gaspar et al., 2013). In order to achieve SPR effect where the nanoparticles polarize, NPs size should be smaller than the wavelength of the incident light. The scattering and absorption of light depends on the polarizability of the NPs, which is a function of the size, refractive index, shape, density and surrounding medium (Gaspar et al., 2013; Huang & El-Sayed, 2010). In order to incorporate the effect of SPR effect using metallic nanoparticles, particularly Ag NPs in electronic applications, in-depth study on the film formation of Ag NPs was carried out. This chapter presents an in-depth study on the parameters that influenced the behavior of Ag NPs. This chapter begins with the experimental observation of different thickness of Ag NPs films, which deposited via electron beam technique. Different time exposure was used to produce different thickness of Ag thin layer. The effect of exposure time was also discussed. Following that, the LSPR effect of different Ag NPs thicknesses on the optical behavior and film surface morphology was observed via UV-Vis absorption and AFM respectively. In this chapter, two different softwares, which are Adaptive Neuro-Fuzzy Inference System (ANFIS) and Finite Domain Time Difference (FDTD) were used to simulate the effect of different parameters and compare it with the experimental results. In addition to that, a model developed using support vector regression (SVR) method was also demonstrated as a prediction of Ag NPs LSPR over a wide range of wavelength.

## 4.2 Results and Discussion

The effect of temperature variation experimental results on Ag NPs behavior was compared with the simulation results from ANFIS software. ANFIS software was also used to predict the absorbance spectra at different thickness. An experiment was carried out to extract the training and checking data for the ANFIS network. This technique gives fuzzy logic the capability to adapt the membership function (MF) parameters that best allow the associated FIS to track the given input/output data (Enayatifar et al., 2013; Grigorie & Botez, 2009; Khoshnevisan et al., 2014). The obtained results are used as training and checking data for a soft computing methodology Support Vector Regression (SVR). SVR was used to construct a process that simulates the resonance spectra in regard to different silver nanoparticles thicknesses in order to estimate the surface plasmons resonance (LSPR) over a wide wavelength range.

### 4.2.1 Influence of temperature exposure to Ag NPs characteristic: A comparative study experimental and simulation

#### 4.2.1.1 Experimental result

A 20 nm thin and homogenous Ag film used in this work was deposited on ITO substrate. It will transform to a layer of particles due to mobility of Ag atoms caused by thermal annealing. As this process continues, holes start to develop and merge and the film gradually transforms into a layer of separated Ag islands with random sizes and shape as shown in Figure 3.3. These phenomena can be seen from FESEM images shown in Figure 4.1. Annealing process at particular temperatures show temperature-specific sizes of granular structures formed on top of the wafer. Figure 4.1(a) to (d) display the changes on an Ag film with temperature increments in the annealing process. This figure demonstrates that Ag films with the annealing process will consequently form regular shapes of Ag particles. Together with the images are distributions of particle diameter that correspond to the formation of Ag particles.

Figure 4.1(a) shows that Ag particles distributed evenly with maximum distribution at ~ 50 nm particle diameters with the smallest diameter range of ~20 nm. Figure 4.1(b) shows the image of Ag particles after thermal annealing at 250 °C. The highest percentage distribution is in the range of 12–15 nm, and the smallest diameter obtained is ~5 nm. Figure 4.1(c) shows that the maximum percentage distribution is ~50 nm with the smallest diameter obtained as 20 nm. However, the smallest diameter recorded here is found to be less than that at temperature annealing of 200 °C. This could be due to particles starting to break up and form a more stable condition at this temperature. At 400 °C (Figure 4.1(d)), particles with clearly bigger and percentage distribution are more well separated, with a diameter ranging from 20 to 120 nm. Some distinct holes appear on the surface at this temperature (400 °C), indicating partial embedding of Ag particles in the substrate during high temperature annealing as reported in past studies (Farzinpour et al., 2012; Kreibig & Vollmer, 2013; Tesler et al., 2011). For this work, thermal annealing is carried out at 250 °C since the smallest diameters corresponding to as small as 5 nm can be obtained and hence confirm this as the most appropriate temperature to transform Ag thin films to Ag particles. Compared to other temperature, the particles are bigger as shown in distribution graph. The particle distribution graph agrees with the variations of the diameter (*D*) of these particles according to Gaussian function (Kreibig & Vollmer, 2013):

$$f(D) = \frac{1}{\sigma\sqrt{2\pi}}\exp(\frac{(D-D_0)^2}{2\sigma^2}) \tag{4.1}$$

where $\sigma$ is standard deviation and $D_0$ is mean of diameter.

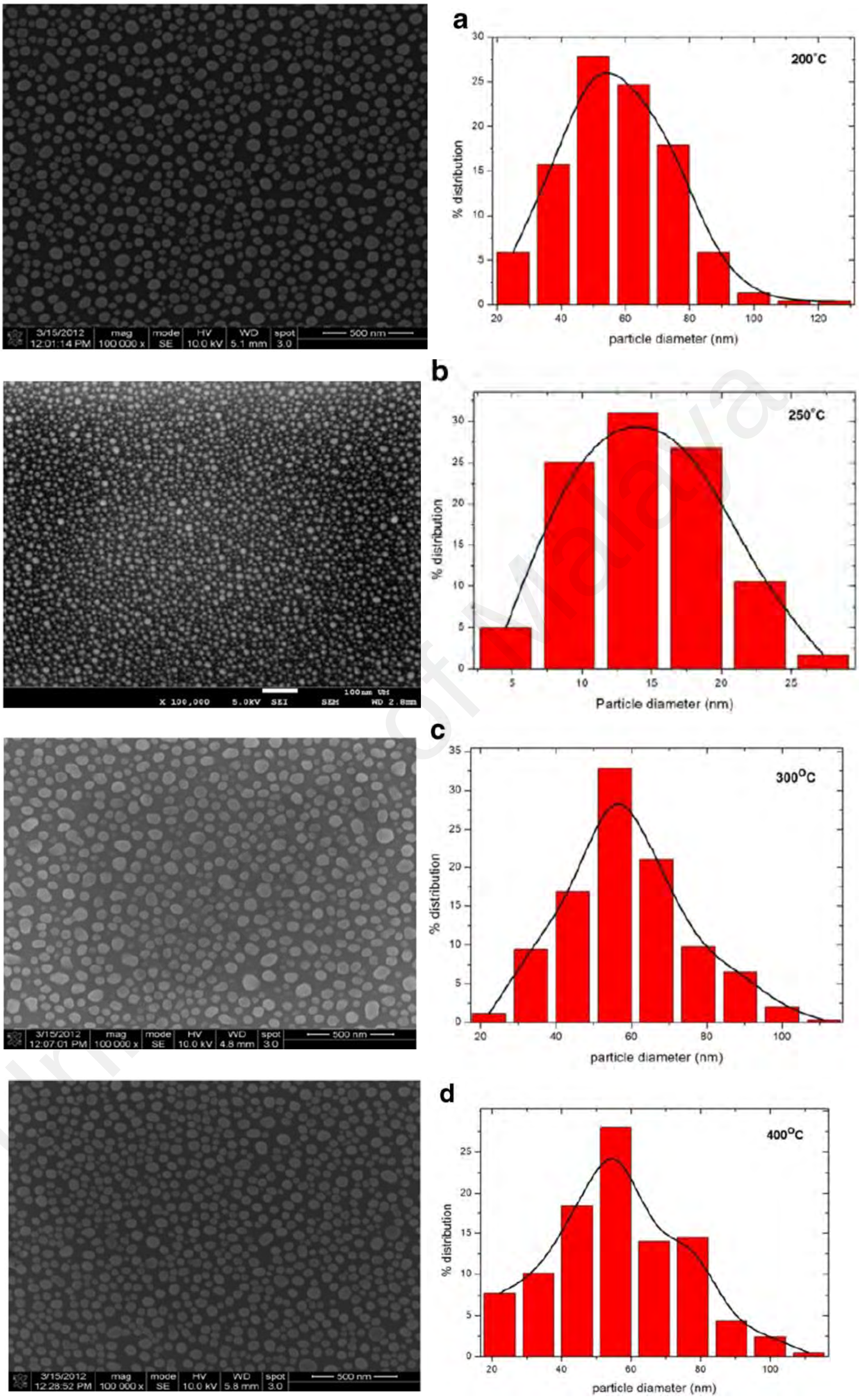

**Figure 4.1:** Field emission scanning electron microscopy (FESEM) graphs distribution and images for (a) 200 °C, (b) 250 °C, (c) 300 °C and (d) 400 °C.

#### 4.2.1.2 Adaptive Neuro-Fuzzy Inference System (ANFIS) simulation result

Fuzzy inference system (Eliezer et al.) is the core of the ANFIS. FIS is based on expertise expressed in terms of "IF–THEN" rules and can thus be employed to predict the behavior of many uncertain systems (Akcayol, 2004). Figure 4.2 shows ANFIS-predicted distributions of particle diameter corresponding to the formation of Ag particles for different thermal annealing. Simulations are run in MATLAB and the results observed on the corresponding output blocks. It can be seen that the distribution increases with increasing Ag particle diameters and for smaller thermal annealing. Initially, the ANFIS network is trained with extracted data from the experimental analysis. Three bell-shaped membership functions are used for each input during the training procedure. It is not appropriate to further increase the number of the membership functions since there are an excess of parameters to estimate. The root mean square error for the ANFIS network is 1.2629.

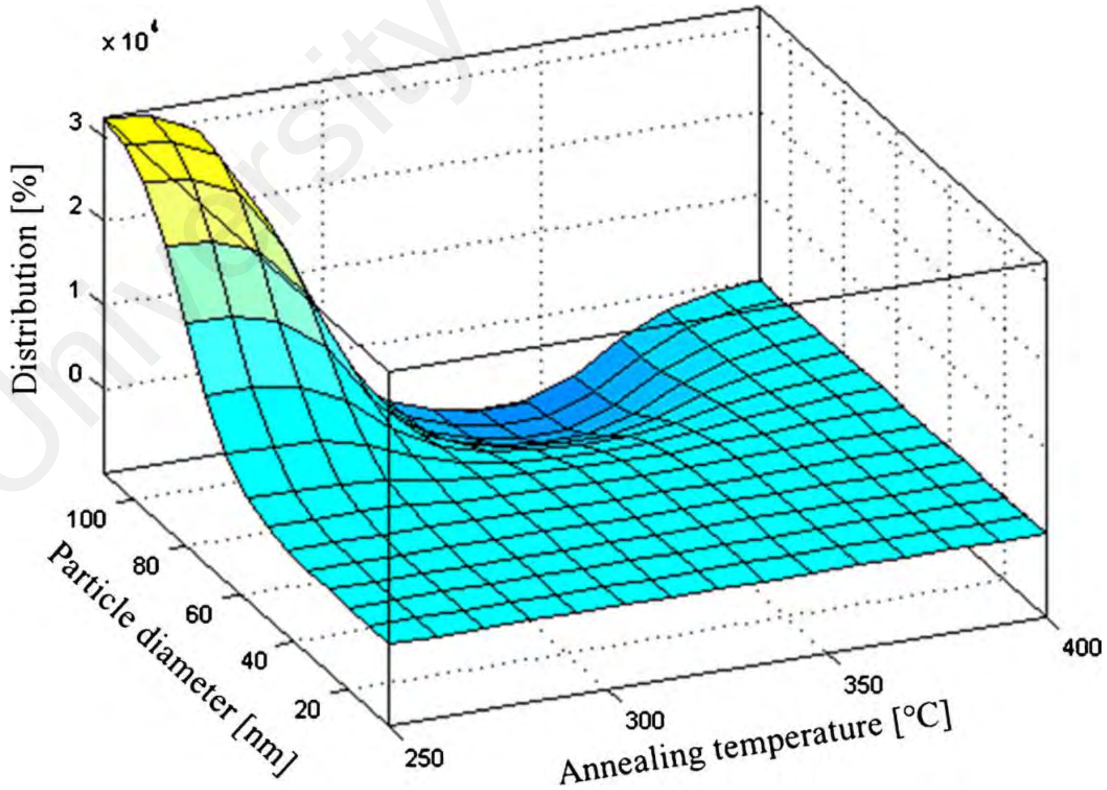

**Figure 4.2:** ANFIS prediction of distribution of different sizes of granular structures at certain annealing temperature**.**

### 4.2.2 Influence of the Ag NPs layer thickness on the coalescence of NPs: Experimental and Simulation

#### 4.2.2.1 Experimental result

Following the optimum temperature (250 °C) obtained from previous section; this optimum temperature was used to observe the thickness effect on the coalescence of nano particles. The thickness for Ag NPs deposition was varied from 20 nm, 30 nm, 35 nm and 45 nm. The distribution and particles size of each thickness was observed using FESEM. Figure 4.3(a) to (d) shows the FESEM image of 20 nm , 30 nm , 35 nm and 40 nm Ag NPs deposited on pre-patterned ITO together with particle diameter and distribution of each thickness. It could be observed that the shape of Ag NPs changed as the thickness of the Ag NPs layer was varied. Annealing process after deposition induces a surface mass transfer between the nanoparticles (Ag islands) resulting the size increases as the film thickness increased. Figure 4.3(a) shows almost perfect spherical shape produced from 20 nm thin films and gradually transformed into a cluster of an island-like shape for 40 nm thin films in Figure 4.3(d). It could also be seen that for 20 nm thick, the particle was randomly distributed all over the substrate. As the thickness of Ag NPs was slowly increased, the particle size gradually become bigger and become a porous film at 40 nm. As shown in particles graph distributions in the right side, the particles size are ranging from 2 nm to ~ 130 nm for all thicknesses. The phenomenon of NPs particle size dependent on mass thickness was also observed by Gaspar et al., 2013).

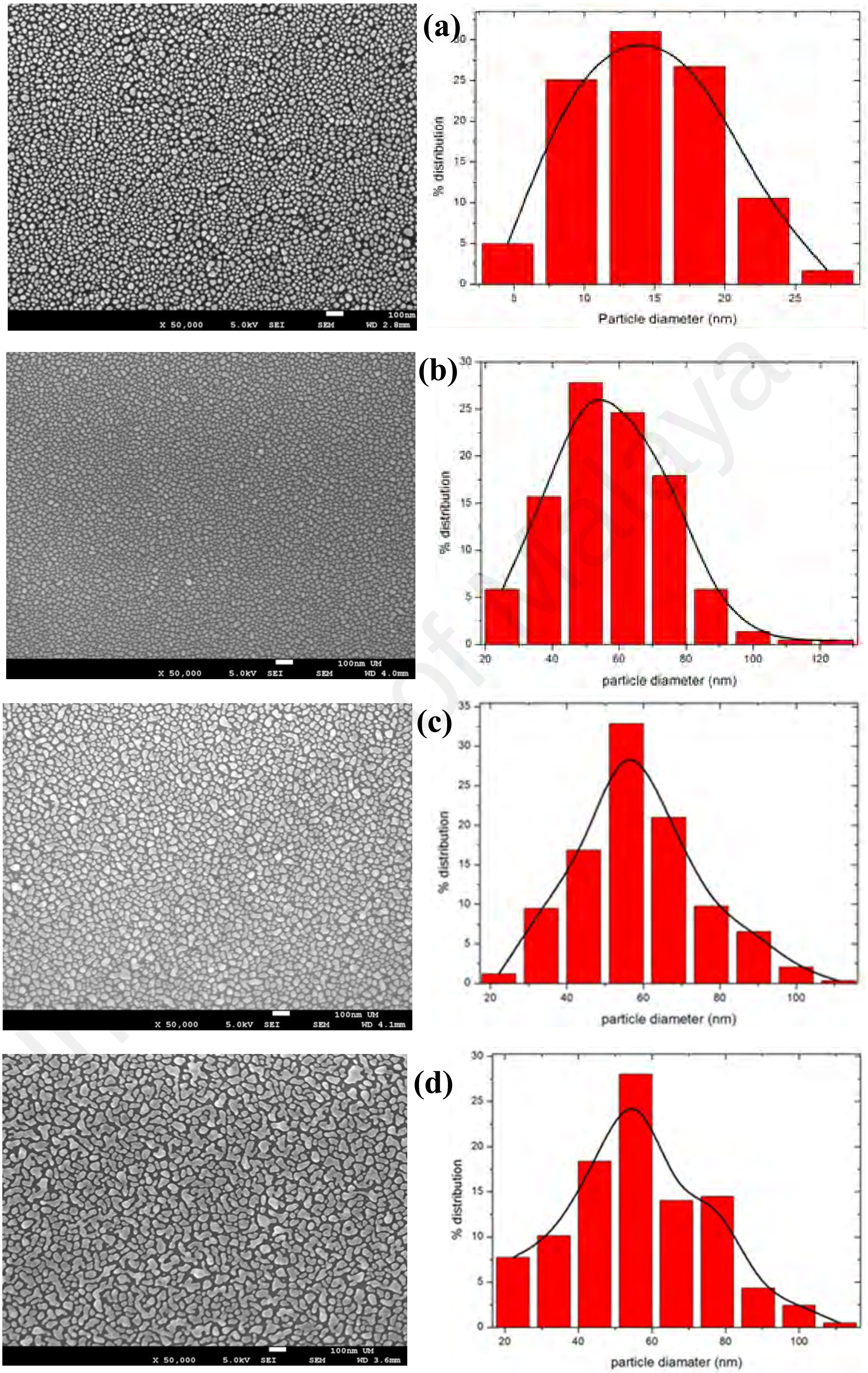

**Figure 4.3:** FESEM with particles size and distribution for (a) 20 nm, (b) 30 nm, (c) 35 nm and (d) 40 nm deposited on pre-patterned ITO.

As could be seen in the Figure 4.3, a thin and continuous Ag film deposited on pre-patterned ITO substrate becomes discontinuous when the Ag atoms in the film become mobile due to thermal annealing. As annealing continues, holes start to develop and merge and the film gradually transform into a layer of separated Ag islands with random sizes and shape (Thompson, 2012). Another observation from FESEM in Figure 4.3 that Ag films exhibits different sizes of granular structures formed on top of the ITO from the annealing. In this experiment, 250 °C is the suitable temperature for Ag film because high temperature could cause the significant silver evaporation. The nanoparticle diameter and inter-particle spacing for each thickness were measured from the FESEM. Figure 4.4 shows that inter particle spacing that was measured according to center-to-center nearest neighbor distances for all thicknesses. This dewetting behavior observed is also consistent with former studies.

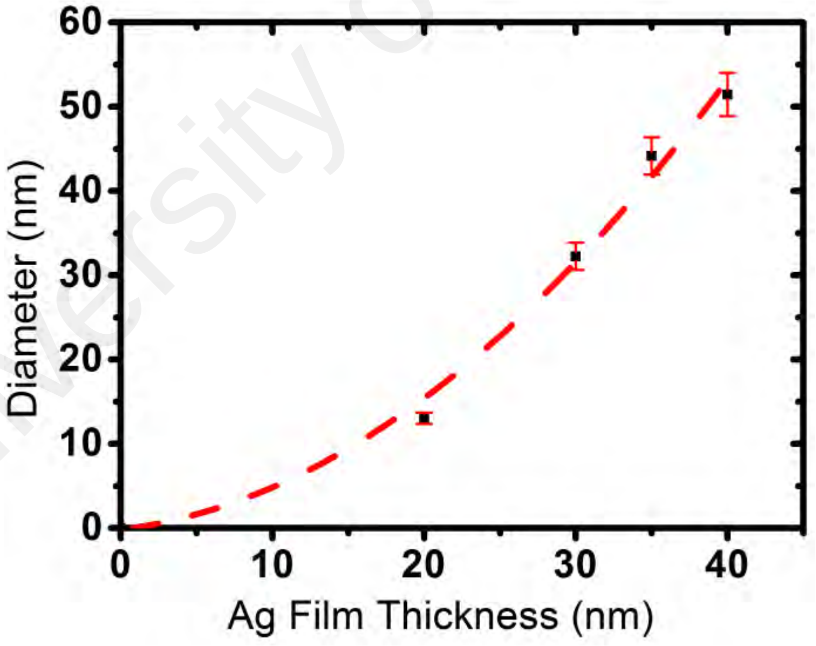

**(a)**

**Figure 4.4:** (a) Ag particle's diameter (b) Ag particle density and (c) Inter particle spacing for 20 nm, 30 nm, 35 nm and 40 nm.

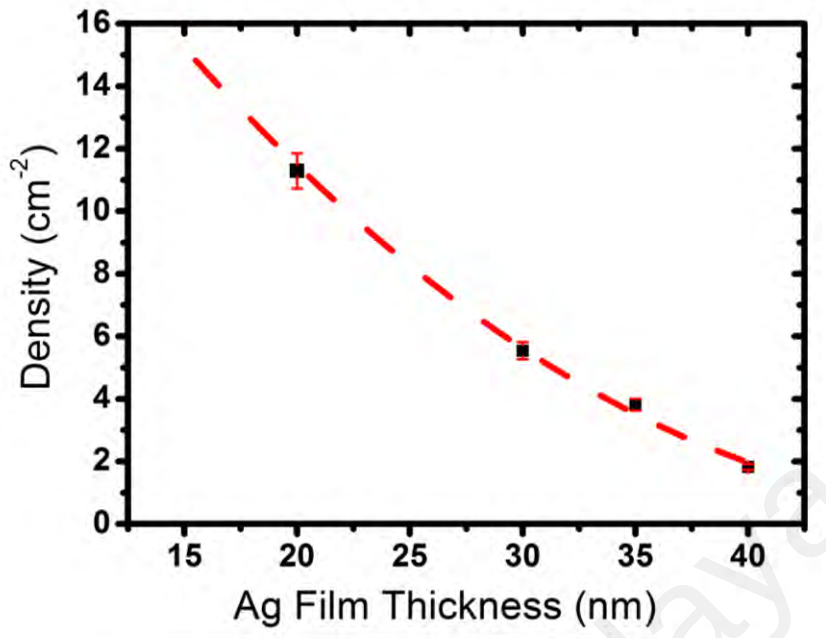

**(b)**

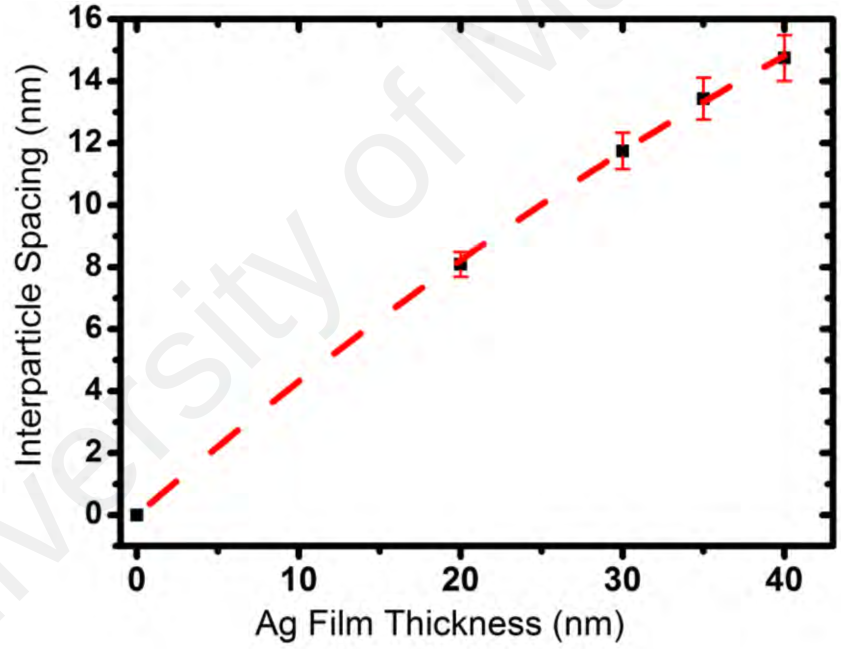

**(c)**

**Figure 4.5:** Continued.

As shown in Figure 4.4(a) and (c), the increment in the diameter of the particle from ~12 nm to 52 nm as well as the inter particles spacing which is ~8 nm to 15 nm occurs simultaneously with the increment of the Ag NPs thicknesses. At temperature of 250 $^0$C, agglomeration might occur. This is where the Ag islands start to experience mass transfers between themselves. Figure 4.4 depicts that for film thickness of 20 nm to 30 nm, the islands are well-separated as there is big space between them and the particles are in round or oval shape (Figure 4.1). When thicker film deposited (35 nm to 40 nm), there might not be enough space for the particles and thus they cannot detach further. Figure 4.4(b) shows the density of the nanoparticles which decreases from ~11 cm$^{-2}$ to 2 cm$^{-2}$ as thickness of Ag NPs deposited increases. The decreasing in the density implies that there is less Ag island formed.

### 4.2.3 Influence of the layer thickness on the surface roughness

The changes in the particles size may also influence the morphology of the films. Atomic Force Microscopy was used to investigate the surface morphology of the Ag NPs. Figure 4.5(a) to (d) shows the 3D (left) and 2D images (right) AFM for 20 nm, 30 nm, 35 nm and 40 nm film thickness respectively. Upon increasing the thickness, it can be observed there is an obvious change in surface morphology. The surface roughness of for 20 nm, 30 nm, 35 nm and 40 nm film can be clearly observed in Table 4.1. The increasing of surface roughness can be correlated to the nano particle size distribution (Tanyeli et al., 2013). The increasing in surface roughness via AFM shown in our work is consistent with the FESEM result. This result implies that the surface roughness of the NPs can be tailored via the mass thickness of the film.

(a) 20 nm

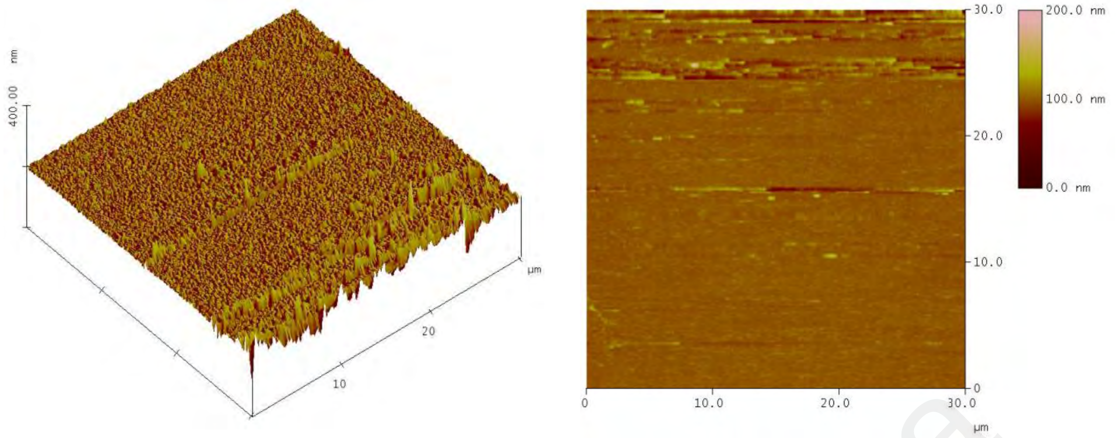

(b) 30 nm

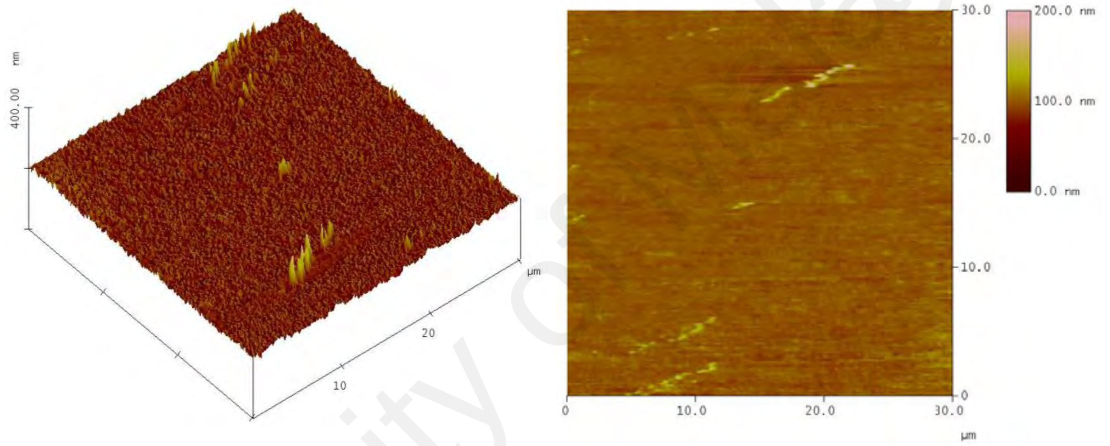

(c) 35 nm

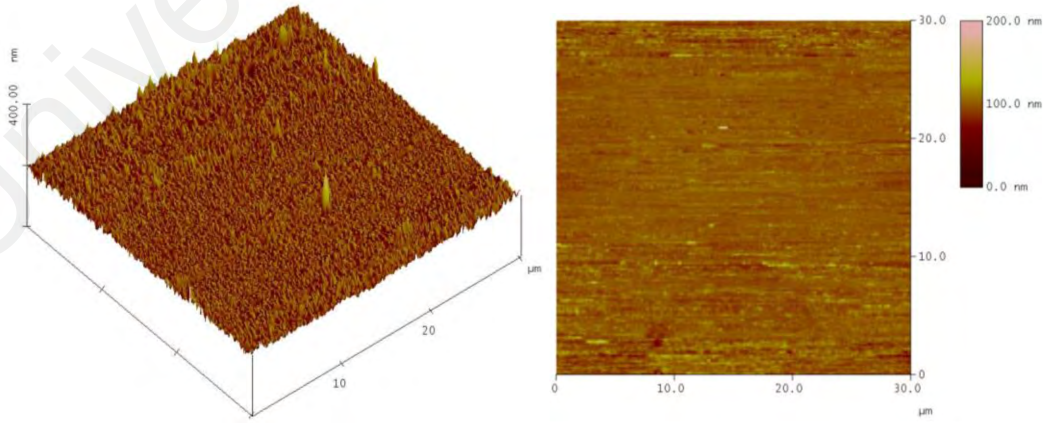

**Figure 4.6:** AFM images of (Left) 3D and (right) 2D for (a) 20 nm (b) 30 nm (c) 35 nm and (d) 40 nm deposited on ITO substrate.

(d) 40 nm

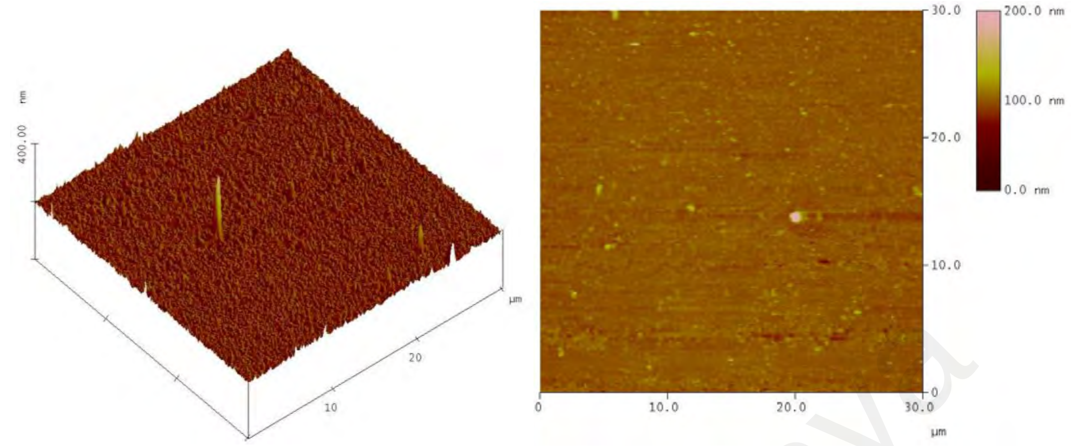

**Figure 4.7:** Continued.

**Table 4.1:** Results obtained from AFM.

| Sample thickness (nm) | Mean roughness (nm) | Maximum height (nm) | RMS (nm) |
|---|---|---|---|
| 20 | 1.758 | 32.155 | 2.387 |
| 30 | 2.660 | 39.865 | 3.550 |
| 35 | 3.401 | 60.849 | 4.162 |
| 40 | 4.589 | 67.287 | 4.589 |

### 4.2.4 Influence of the layer thickness on UV-Vis absorption: Experimental and Simulation

#### 4.2.4.1 Experimental results

The variability of Ag NPs structure's sizes and shapes as shown in previous results provide effective means of tuning the position of the localized surface plasmons resonance (LSPR) in wide wavelength range. To investigate the LSPR effect, the absorption spectrum of Ag NPs films was measured using UV-Vis spectroscopy. Figure 4.6 shows the absorption of each thickness of Ag NPs produced.

Figure 4.6 illustrates that the peak of 20 nm located at ~ 425 nm and it can be observed that the peak shift to higher wavelength as the mass thickness of Ag NPs increased up to 30 nm which is at ~ 450 nm. The peak is red shifted at 461 nm when the thickness increased to 35 nm and 488 nm at 40 nm film thickness. The broadening of the peak can also be correlated to the enlargement of the NPs as shown in FESEM images in Figure 4.1.

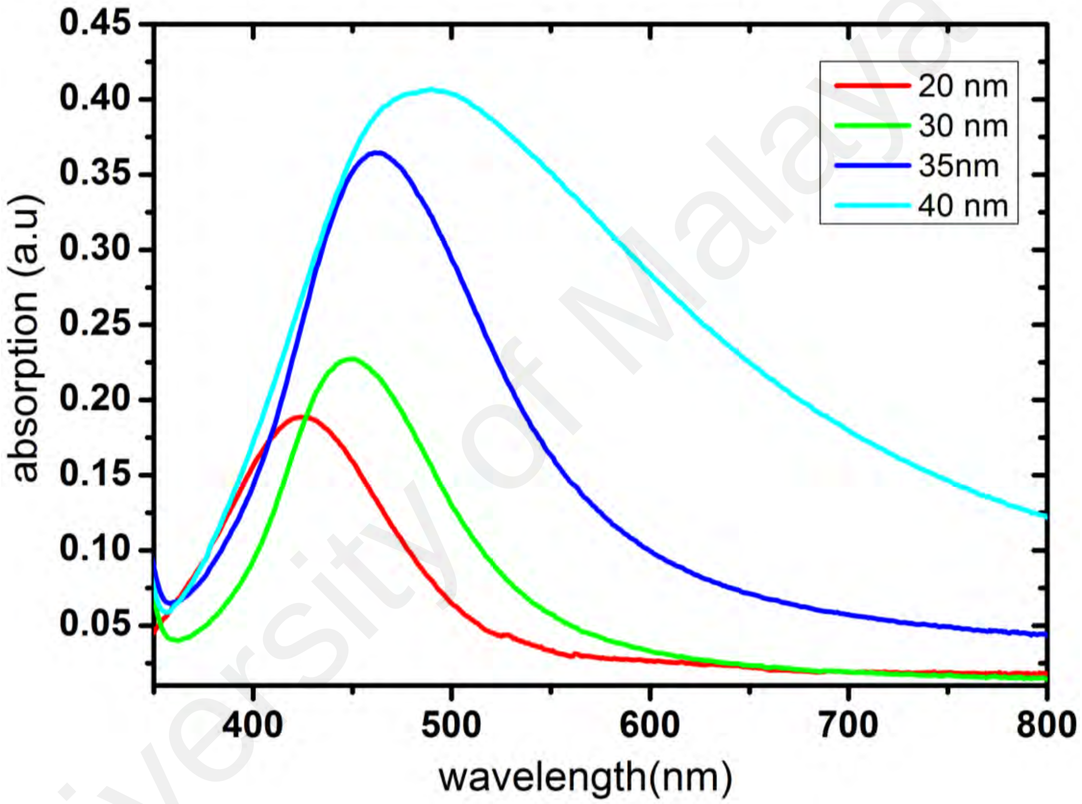

**Figure 4.8:** Absorption spectrum of Ag nanoparticles from UV-Vis.

There have been reports on the effect of size, density as well as the NPs shape of NPs on the plasmonic peak (Thompson, 2012). Halas et al., 2011 explained that a sharp plasmonic peak for Au spherical NPs shows a red shift due to inter-particle coupling (Halas et al., 2011). If the distance two particles are close enough, they can form a plasmonic dimer with a red shift that depending on the distance interaction between these particles (Hao & Schatz, 2004; Jain et al., 2007; Lassiter et al., 2008). This phenomenon represents the near field interaction between two close metallic NPs where their s- and p- polarization is influenced by the separation and size (Carl V. Thompson, 2012). In addition to that, it can be observed that the intensity of the peak is gradually increased as the thickness of Ag NPs film increased. This can also attributes to the increasing of particles diameter, which is consistent with the FESEM images shown in Figure 4.1. It also reported that the absorption of semiconductor enhanced as it become closer to an electric field of an emitting dipole. In the other words, it can be originated by the enhancement of electric field around the surface plasmons (Huang & El-Sayed, 2010).

The characteristic of plasmonics can also be obtained from theoretical calculation. Gustave Mie has first introduced the classical Mie's theory where the particles and surrounding medium interact in bulk optical dielectric function (Haiss et al., 2007; Kelly at al., 2003). Discrete dipole approximation (DDA) (Félidj, Aubard, & Lévi, 1999; Jain et al., 2006), finite difference time domain (FDTD) (Futamata et al., 2003; Gray & Kupka, 2003; Oubre & Nordlander, 2004), and modal expansion techniques are commonly used to simulate the absorption spectra. In this experiment, the resonance spectra were obtained using Finite Domain Time Difference (FDTD) for numerical simulations software shown in Figure 4.7

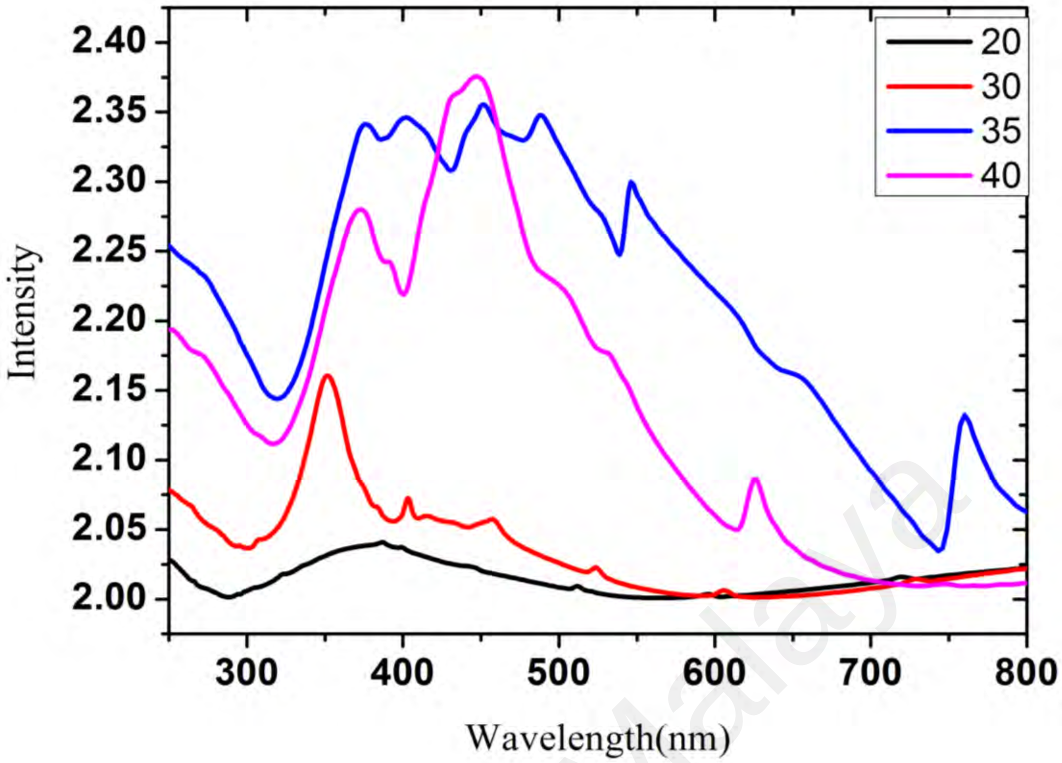

**Figure 4.9:** Absorbance spectra simulated from FDTD of silver nanoparticles.

Figure 4.7 illustrates that for 20 nm Ag NP film thickness, a broad absorbance spectrum appears with an absorbance peak at around 388 nm and intensity around 2.04. As the film thickness increases to 30 nm, the absorbance peak sharpens and blue-shifted to around 351 nm and intensity rose to 2.16. There are two dominant absorbance peaks for 40 nm films and redshift with respect to the 30 nm film. However, the peak intensity for 35 nm Ag NPs film is higher than the 40 nm Ag film. In addition to that, there are some trends that can be noticed for up to three film thicknesses where the absorbance peak increases as the film thickness increase. It can be conclude that, the results obtained from FESEM are comparable with calculated results from FDTD.

#### 4.2.4.2 ANFIS simulation result

Extracting the simulation result conducted using FDTD software (Figure 4.7) whereby the original image obtained from FESEM (Figure 4.3) were imported to the software, and the extracted data is used for ANFIS training. The root mean square error for the ANFIS network is 0.02061. The final calculated surfaces following a training procedure of the ANFIS network are shown in Figure 4.8, and these represent the resonance peak of SPR prediction from the absorbance spectra. Some trends from the graph can be noticed where the absorbance peak increases as the film thickness increase. The magnitude of the absorption spectra also decreases at longer wavelength. The resultant spectrum from ANFIS is consistent with the experimental results from UV-Vis equipment.

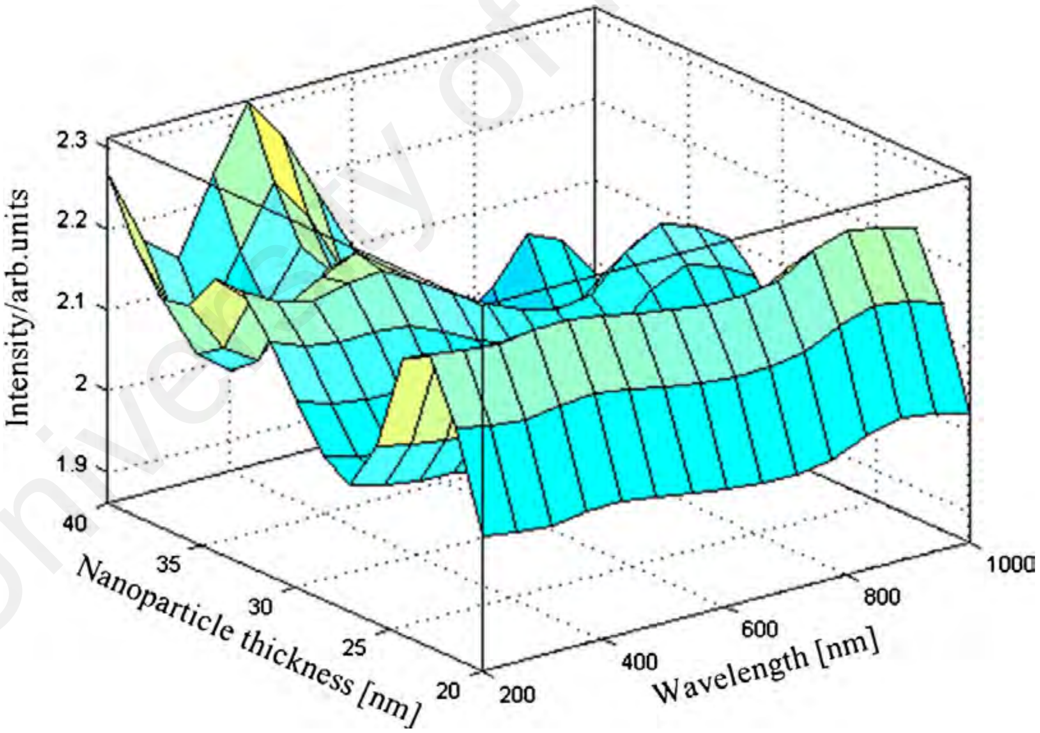

**Figure 4.10:** ANFIS prediction of absorbance spectra of silver nanoparticles at thickness 20 nm to 40 nm.

The increase in the absorption to near-infrared wavelength is adequate for OLED applications. The size and the spacing between the NPs and the emitter are important parameters in term of matching the LSPR with the maximum emission frequency of the OLED. The application of Ag NPs in OLED device is explained in the next chapter.

### 4.2.5 Support vector regression (SVR) method to estimate the surface plasmons resonance (LSPR) of Ag NPs over the wavelength

In addition to the result obtained using ANFIS and FDTD, the support vector regression (SVR) methodology is also used to estimate of the LSPR over a broad wavelength range by a process in which the resonance spectra of silver nanoparticles differing in thickness. The core idea behind the soft computing methodology is to collect input/ output data pairs and to learn the proposed network from these data (Javanmardi et al., 2014; Pooranian et al., 2015). The key goal of this investigation is to establish an approximated support vector regression (SVR) methodology for forecasting and estimation of the LSPR over a broad wavelength range. An attempt is made to retrieve correlation between different thicknesses of silver nanoparticles in regard to surface plasmon resonance.

There are two main categories to support vector machines: support vector classification (SVC) and support vector regression (SVR). SVM is a learning system using a high dimensional feature space (Balahur & Turchi, 2014). The Support Vector Regression algorithms (SVR) specifically developed or regression problems are appealing algorithms for a large variety of regression problems, since they do not only take into account the error approximation to the data, but also the generalization of the model, which is their capability to improve the prediction of the model when new data are evaluated by it (Rajasekaran et al., 2008; Yang et al., 2009). SVR is based on statistical learning theory and a structural risk minimization principle, which has been successfully used for non-linear system modeling (Zhang et al., 2013). The accuracy of a SVM model is largely dependent on the selection of the model parameters. However, structured methods for selecting parameters are lacking. Consequently, some kind of model parameter calibration should be made. The SVR_rbf and SVR_poly are examined in this thesis. The first one is radial basis function (RBF) and the later is polynomial (POLY) function. These functions represent kernel functions, which are utilized to form qualified function for SVM. Hence, the RBF and polynomial function are applied or estimation of sensor voltage output in this study.

In this thesis work, SVR training and checking data were acquired by presented experimental and simulation procedure shown in previous sections. The simulation was conducted using FDTD software where by the original image obtained from FESEM was imported to the software, and the extracted data was used for SVR training. Some trends from the graph can be noticed where the absorbance peak increases as the film thickness increase. The magnitude of the absorption spectra also decreases at longer wavelength.

#### 4.2.5.1 Input parameters

As a data-driven model, the ability of the SVR to make reasonable estimations is mostly dependent on input parameter selection. Adequate consideration of the factors controlling the system studied is therefore crucial to develop a reliable network. According to the presented experimental analyzing of the plasmon resonance shown previously, the input parameters annealing temperature and particle diameter are collected and defined as input for the learning techniques. The output data are sizes of granular structures distribution. For the experiments, 70 % of the data was used to train samples and the subsequent 30 % served to test samples. A summary of the statistical properties of the plasmon resonance is provided in Table 4.2. The standard deviation in the tables represents the distribution of the responses around them mean. It indicates the degree of consistency among the responses.

**Table 4.2:** Statistical properties of experimental data of the surface plasmon resonance**.**

| **Input parameter** | **Average value (x)** | **Standard deviation (σ)** | **Maximum value ($X_{max}$)** | **Minimum value ($X_{min}$)** |
|---|---|---|---|---|
| Annealing temperature [$^{o}$C] | 325 | 250 | 400 | 250 |
| Particle diameter [nm] | 53.98 | 106.56 | 111.11 | 4.55 |

### 4.2.5.2 SVR result analysis

To evaluate the performance of the SVR_rbf and SVR_poly model, several measures were used to confirm the validity of the proposed SVR models. The root mean squared error (RMSE) served to evaluate the differences between the expected and actual values. The parameters are calculated as indicated in Table 4.3, where n is the total number of test data, $d_i$ is experimental value and $y_i$ is forecast value. $\overline{d_i}$ is averaged experimental value and $\overline{y_i}$ is averaged forecast value. 1/3 of the testing data set was used to validate the proposed model.

**Table 4.3:** Performance criteria

| **Criteria** | **Calculation** |
|---|---|
| Root Mean Square Error (*RMSE*) | $RMSE = \sqrt{\frac{1}{n}\sum_{i-1}^{n}(d_i - y_i)^2}$ (4.2) |
| Correlation Coefficient (*R*) | $R = \frac{\sum_{i-1}^{n}(d_i - \overline{d_i})(y_i - \overline{y_i})}{\sqrt{\sum_{i-1}^{n}(d_i - \overline{d_i})^2 \sum_{i-1}^{n}(y_i - \overline{y_i})^2}}$ (4.3) |

Radial basis function (RBF) was applied as the Kernel function for discharge prediction in this study. The three parameters associated with RBF Kernels are *C*, *e* and *r*. SVM model accuracy is principally dependent on model parameter selection. In our scheme, a default value of $e$ = 0.001 seemed to perform well. To select user-defined parameters (i.e. *C*, *d* and *g*), a large numbers of trials were carried out with different combinations of *C* and d for polynomial kernels and *C* and *g* for radial basis function kernels. Table 4.4 provides the optimal values of user-defined parameters for this data set with polynomial and RBF kernel-based SVR. For reasonable appraisal of outcomes with both RBF and polynomial kernels, a similar parameter *e* value was applied with SVR.

**Table 4.4:** User-defined parameters for SVR_rbf and SVR_poly for LSPR prediction.

| **Linear kernel** | | | **RBF kernel** | | | **Polynomial kernel** | | | | |
|---|---|---|---|---|---|---|---|---|---|---|
| *C* | *e* | *t* | *C* | *e* | *t* | $\gamma$ | *C* | *e* | *t* | *d* |
| 2000 | 0.001 | 0.1 | 5000 | 0.01 | 0.02 | 0.02 | 500 | 0.001 | 0.01 | 1.0 |

The initial, original data helped establish the polynomial and RBF kernel-based SVR. The data was essentially predicted using SVR -based RBF and polynomial. The results of RMSE of the SVR_rbf, SVR_poly and SVR_lin, models are presented in Figure 4.9 in terms of training and testing for the plasmon resonance. The results in Figure 4.9 show the linear relationship of models with real data to illustrate the capability of models for prediction. The SVR_rbf model has very small RMSE during training and the value was increased in testing. On the other hand, the SVR_poly has RMSE larger in the training phase and smaller in testing phase. It is observed that, the SVR_poly model showed consistently good correlation throughout training and testing.

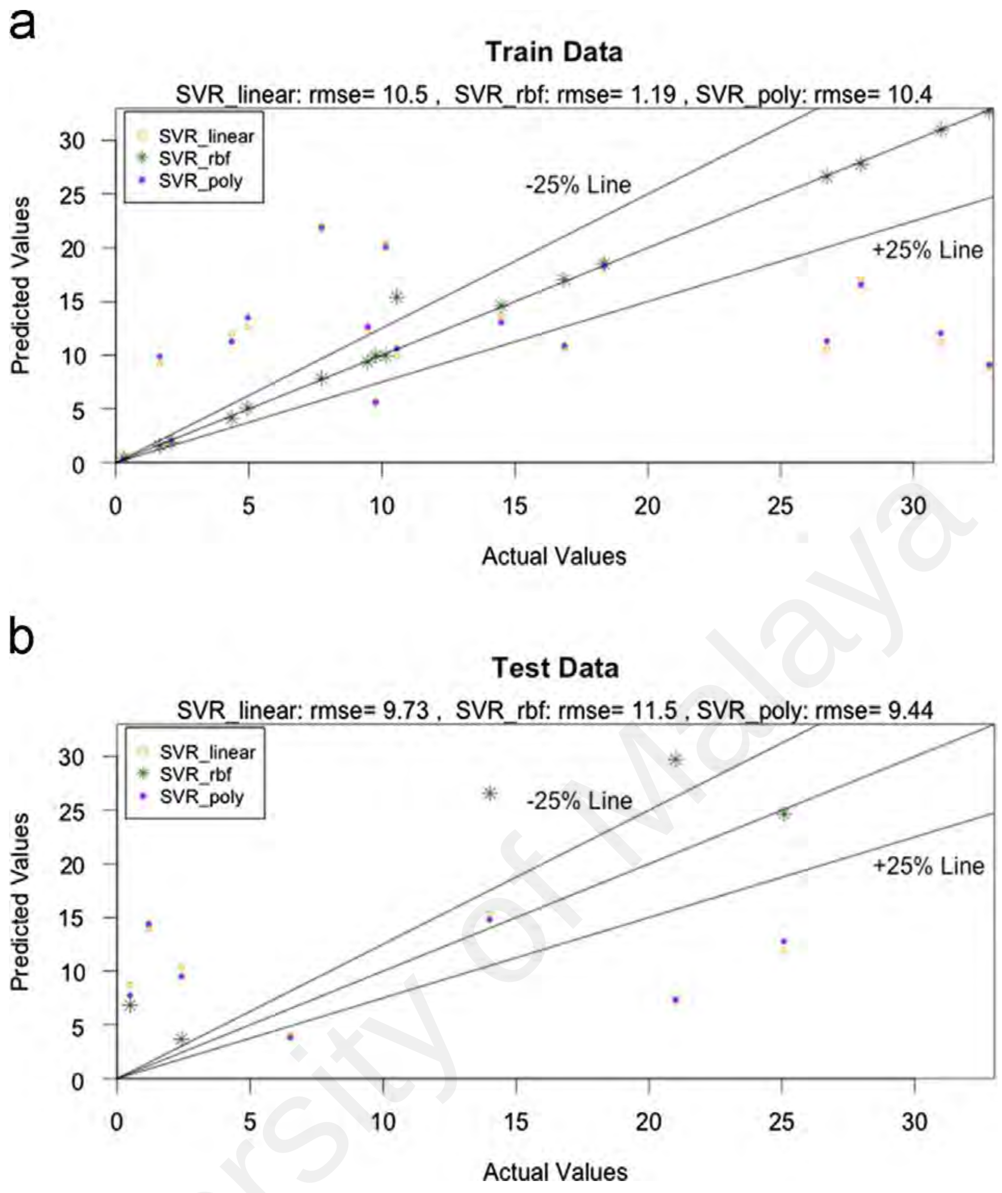

**Figure 4.11:** Plot of observed and predicted sensors output with plasmon resonance estimation with the original data set using SVR_rbf, SVR_poly and SVR_lin model during training (a) and testing (b).

To evaluate SVR model performance, observed equilibrium of input values were plotted against the predicted plasmon resonance. Due to the small sample size, the data set was split into training and testing (70/30 as a fair split). Figure 4.9(a) illustrates the results with the performance indices between observed and predicted data in the training phase, while Figure 4.9(b), indicates the results for the testing phase, respectively. Although the performance of SVR_rbf and SVR_poly in the testing phase is not on a par with other sides, due to the small number of samples data, the optimal kernel function type of SVR is RBF in the dataset. Generally speaking, as seen from Figure 4.9, SVR_poly performed well in predicting of the plasmon resonance. Comparing SVR_rbf results with SVR_poly, reveals that SVR_rbf outperforms the POLY model in terms of prediction accuracy in training phase.

To evaluate the performance of the proposed method experiments were conducted to determine the relative significance of each independent parameter on output. The root mean squared error (RMSE) and correlation coefficient (*R*) served to evaluate the differences between the expected and actual values for SVR_poly, SVR_rbf and SVR_lin. Results in Table 4.5 compares the SVR_rbf, SVR_poly and SVR_lin models. The results in Table 4.5 indicate that the SVR_rbf has the most significant effect on the sensors output estimation for the different concentration of calcium hypochlorite.

**Table 4.5:** Performance indices of various approaches for sensors output prediction without silver coating.

| **Method** | **Training** | | **Testing** | |
|---|---|---|---|---|
| | **Error (RMSE)** | **Correlation coefficient (R)** | **Error (RMSE)** | **Correlation coefficient (R)** |
| SVR_rbf | 1.19 | 0.993648026060382 | 11.5 | 0.161023536976264 |
| SVR_poly | 10.4 | 0.268520388734987 | 9.44 | 0.623182681209909 |
| SVR_lin | 10.5 | 0.993648026060382 | 9.73 | 0.623182681209909 |

An improvement in predictive accuracy and capability of generalization can be achieved by our proposed approach, which results were in agreement with the experimental results show. Results show that SVR can serve as a promising alternative for existing prediction models. It can be seen from the experiment that the prediction model overcomes the main shortage of artificial neural network without defining network structure and trapping in the local optimum.

# CHAPTER 5: SILVER NANO PARTICLES (AG NPS) APPLICATIONS IN OLED DEVICE

## 5.1 Introduction

Following the in-depth analysis of Ag NPs optical characteristic in Chapter 4, the work was then preceded with the fabrication of the organic light emitting diodes (OLEDs) applications. Detailed on the experiments fabrication were explained in Chapter 3. In this chapter, two different colors of OLED devices were demonstrated, which are green and red electrophosphorescent. The Ag NPs films were incorporated into OLED device as hole injection layer (Linic et al., 2011) for Tris[2-(p - tolyl)pyridine] iridium (Morfa et al., 2008) ($Ir(mppy)_3$), and Iridium (Morfa et al., 2008) bis(2-(2'-benzo-thienyl)pyridinatoN,C3')(acetyl-acetonate) ($Ir(piq)_2acac$) which are green and red emitter respectively. Ag NPs were deposited on top of ITO substrates prior spin coating PEDOT:PSS and the active layer. The efficiency for the device with and without Ag NPs was compared. Before carrying out the OLED fabrication, the spectra of Ag NPs and emitters for OLED device were properly examined.

It is well known that LSPR results in the modification of the photophysical characteristics that are the radiative and the non-radiative decay of adjacent emitters (Giannini et al., 2010; Kühn et al., 2006). Two competitive processes can occur. The first one is the radiation intensity enhancement induced by the interaction between surface plasmons and also the fluorophore and the non-radiative quenching of activated fluorophores on the metal surface. Thus, to achieve an overall enhancement of the resonance energy of the fluorophoe, the LSPR should be carefully adjusted (Ford & Weber, 1984; Geddes & Lakowicz, 2002).

## 5.2 OLED device performance

### 5.2.1 LSPR peak for green electrophosphorescent OLED device

Figure 5.1 shows the absorbance of Ag NPs with different thickness range from 5 nm to 25 nm. Noted that the thickness of Ag NPs in this section was varied at small range compared to previous section. This is due to the surface uniformity for good electrical contact. As previously shown in Chapter 4 Figure 4.3, 20 nm Ag NPs exhibits better particle size uniformity compared to other thicknesses. Increasing the Ag NPs thickness also increased the surface morphology. A rough surface morphology could result in a poor electrical contact with the adjacent layer. Thus, in order to maintain a good surface uniformity, Ag NPs were varied below 20 nm. Figure 5.1 illustrates that using 20 nm Ag NPs could results in the optimum behavior for OLED device with the highest absorption peak that overlap with Ir(mppy)$_3$ emitter (Photoluminescence) PL spectra.

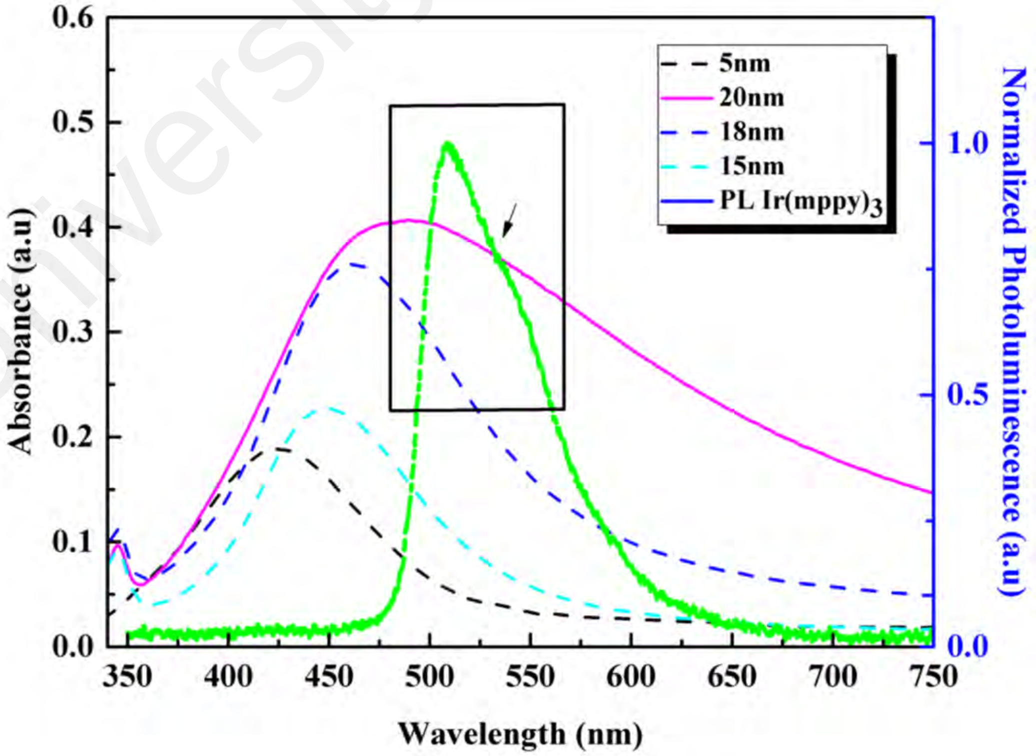

**Figure 5.1:** Overlapping Ir(mppy)$_3$ PL with absorption spectrum of 20 nm film.

It could be seen that the spectra for 20 nm Ag NPs indeed covers the range of Ir(mppy)$_3$ PL emission spectra. The overlap of these two spectra suggests that there might be a possible resonance radiated light generated in Ir(mppy)$_3$ and localized SP excited by Ag NPs (Xiao et al., 2012), which may result in the enhancement of emission intensity of the Ir(mppy)$_3$.

It is demonstrated in literature that by incorporating NPs in hole injection layer (Linic et al., 2011); PEDOT:PSS, the device performance could be increased due to the increase in spontaneous emission rate due to the plasmonic near-field effect induced by metal NPs (Xiao et al., 2012). However, incorporating metal NPs directly into PEDOT:PSS may results in non radiative quenching of activated fluorophores on the metal surface. Placing metal NPs underneath the active layer shown to degrade the device performance due to a massive light loss caused by Ag NPs scattering and absorption (Liu & Nunzi, 2012). In order to prevent a direct contact between metal and organic layer, PEDOT:PSS was spin coated on top of the Ag NPs. Capping PEDOT:PSS on top of metal NPs could prevent excitons quenching on the NPs surface.

Figure 5.2 shows the absorbance of 20 nm Ag NPs with PEDOT:PSS layer on top of it. When PEDOT:PSS was spin coated on top of the Ag NPs, the shifting of absorbance spectra ~ 486 nm to ~ 498 nm could be observed. This result is consistent with the literature where by adding PEDOT:PSS on top of metal NPs, the absorbance spectra of the Ag NPs would also be shifted (Kim et al., 2014).

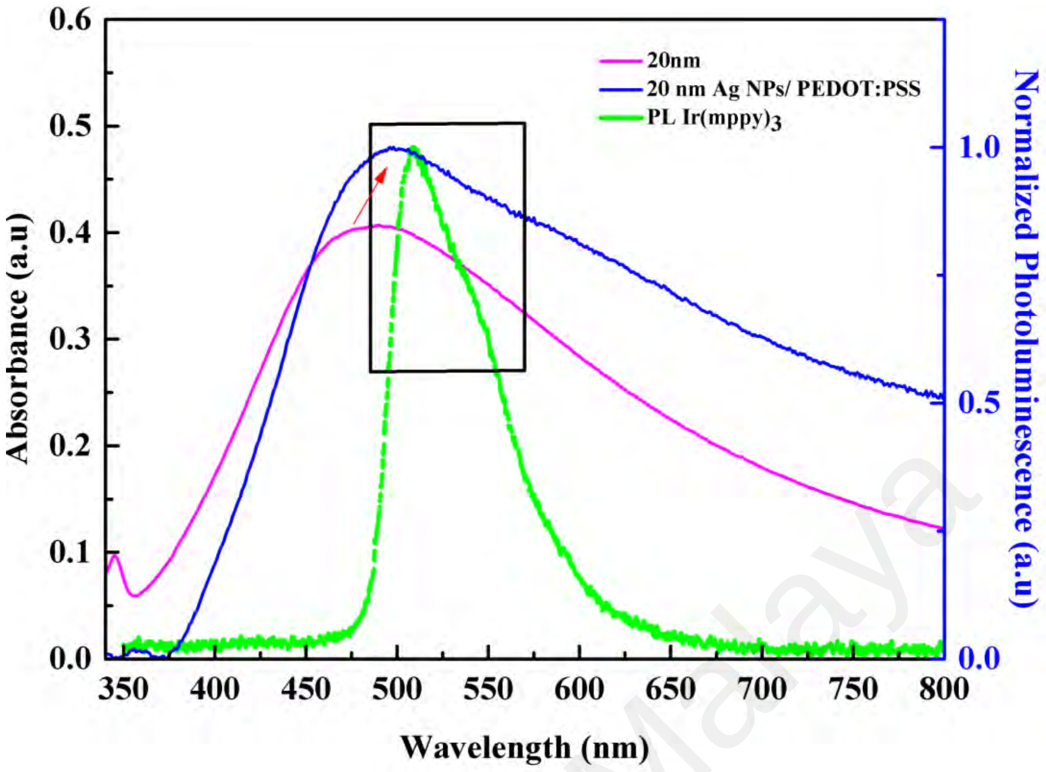

**Figure 5.2:** Absorbance spectra shifted when PEDOT:PSS spin coated on top of Ag NPs.

Based on the Mie's theory where:

$$\sigma_{ext}(\lambda) = \frac{24\pi N_A a^3 \varepsilon_m^{3/2}}{\lambda \ln(10)} \left[ \frac{\varepsilon_i}{(\varepsilon_r + \chi\varepsilon_m)^2 + \varepsilon_i^2} \right] \tag{5.1}$$

where $N_A$ is the areal density of nanoparticles, a is the radius of the metallic nanoparticles, $\varepsilon_m$ is the dielectric constant of the medium surrounding the metallic nanosphere (assumed to be a positive, real number and wavelength independent), $\lambda$ is the wavelength of absorbing radiation, $\varepsilon_i$ is the imaginary component of the metallic nanoparticle's dielectric function, and $\chi$ is the term that describes the aspect ratio of the nanoparticle (equal to two for a sphere). It is clear that the LSPR spectrum of an isolated metallic nanosphere embedded in an external dielectric medium will depend on the nanoparticle radius $a$, the nanoparticle material ($\varepsilon_i$ and $\varepsilon_r$), and the environment's dielectric constant ($\varepsilon_m$).

The resonance occurs where the real part of dielectric constant Ag NPs $\varepsilon_1(\omega)$ is equal to $2\varepsilon_m$, where $\varepsilon_m$ is the dielectric constant of air or PEDOT:PSS. With $\varepsilon_m$ being positive, the Ag NPs have negative dielectric constant. Also the observed resonance red shift is expected by the equation, as the dielectric constant of surrounding material (PEDOT: PSS) is greater than that of air. The red shift of Ag NPs absorbance in Figure 5.2 is in consistent with the theory. The spectra shifting to ~ 498 nm results in a better the spectra overlap between Ag NPs absorbance and PL spectra of $Ir(mppy)_3$.

### 5.2.2 Green Electrophosphorescent OLED device efficiency

Figure 5.3 shows the current density of the OLED device corresponds to the voltage used. The device with Ag NPs exhibits lower current density compared to the device without Ag NPs. To get 20 mA, the device without Ag NPs only requires driving voltage of 3 V, but the device with Ag NPs needs more than 10 V. This may attribute to the charge carrier that was captured and trapped at Au NPs sites. Other possibility for the reduction of charge carrier in Ag NPs device might due to the particle size of Ag NPs. As shown in FESEM result, the particles size of 20 nm is around ~20 nm. Das et al. demonstrated that the current density of 3 nm NP in the device dropped compared to 1 nm NP which may result from the fact that a larger size Ag-NPs have smaller curvature thus less local electrical field amplification (Das et al., 2011).

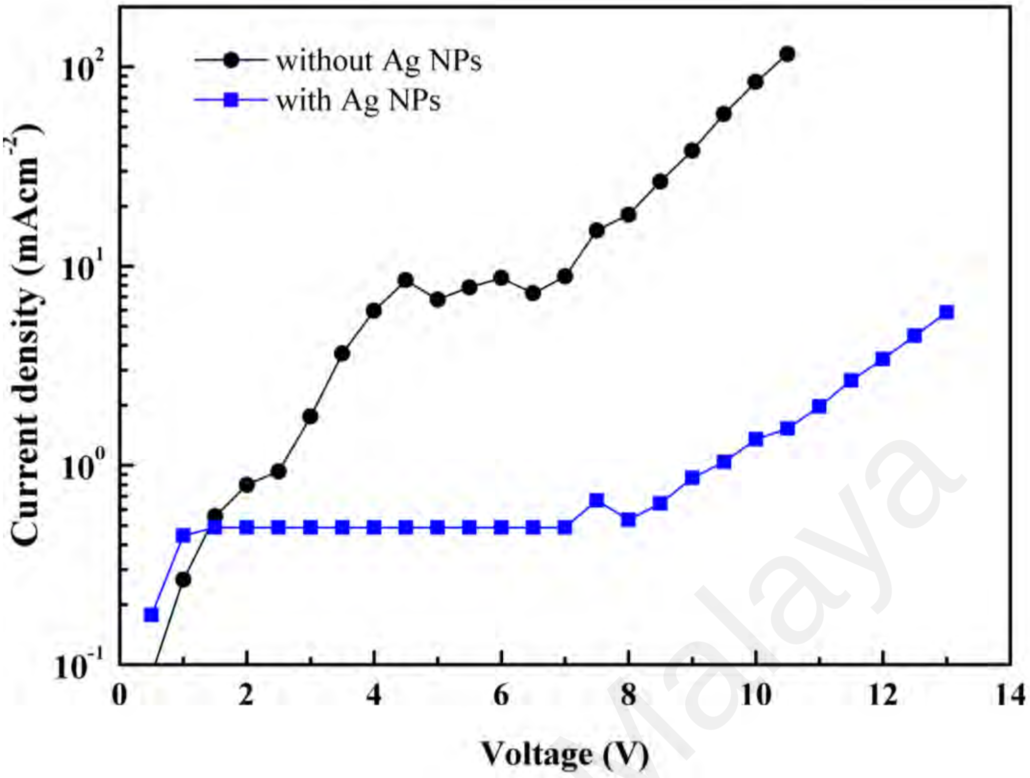

**Figure 5.3:** Current density versus Voltage (J-V) for OLED based Ir(mppy)$_3$ as emitter.

Figure 5.4 illustrates the energy level of the fabricated green device. It is shown that Ag NPs work function is 4.70 eV while PEDOT:PSS exhibits 5.20 eV energy level. This implies that hole carrier need to overcome ~0.6 eV barrier in order to be injected into PEDOT:PSS. A significant hole injection barrier between Ag NPs and PEDOT:PSS interface with Ag NPs acting as charge (hole) trap, hindering the hole injection from ITO to the active layer. These results in the low current density of the device with Ag NPs compared to the device without Ag NPs.

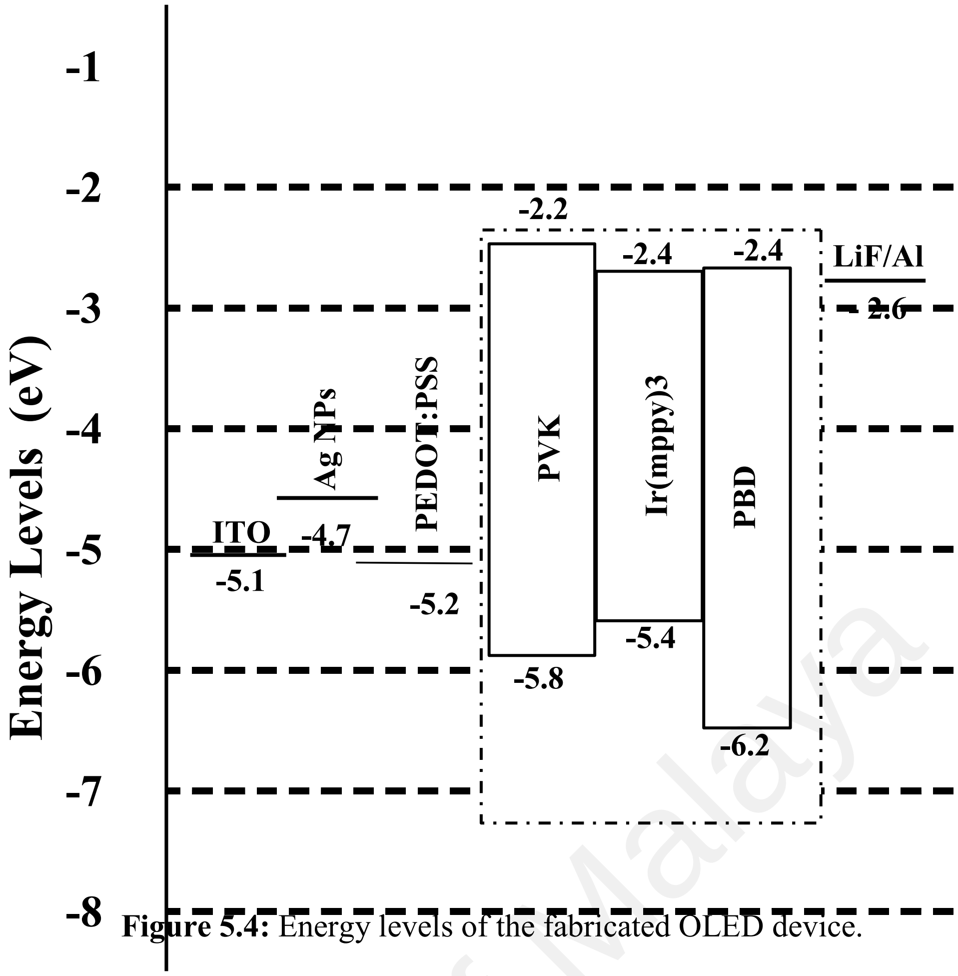

**Figure 5.4:** Energy levels of the fabricated OLED device.

However, instead of lower current density for the Ag NPs based device, the device efficiency for the device with Ag NPs device is enhanced as shown in Figure 5.5. At 1000 cd/m$^2$, the efficiency for the device with Ag NPs is 18.8 cd/A with 4.96 lm/W, while the device without Ag NPs exhibits 5.32 cd/A with 2.04 lm/W for current efficiency and power efficiency respectively. This implies that by incorporating the Ag NPs the device enhancement achieved is more than 3 folds than that of the device without Ag NPs. The enhancement is attributed to the charge balance in emissive layer was achieved by reducing the hole injection by Ag NPs. The enhancement also may due to the increasing in spontaneous emission rate due to the plasmonic near-field effect induced by Ag NPs.

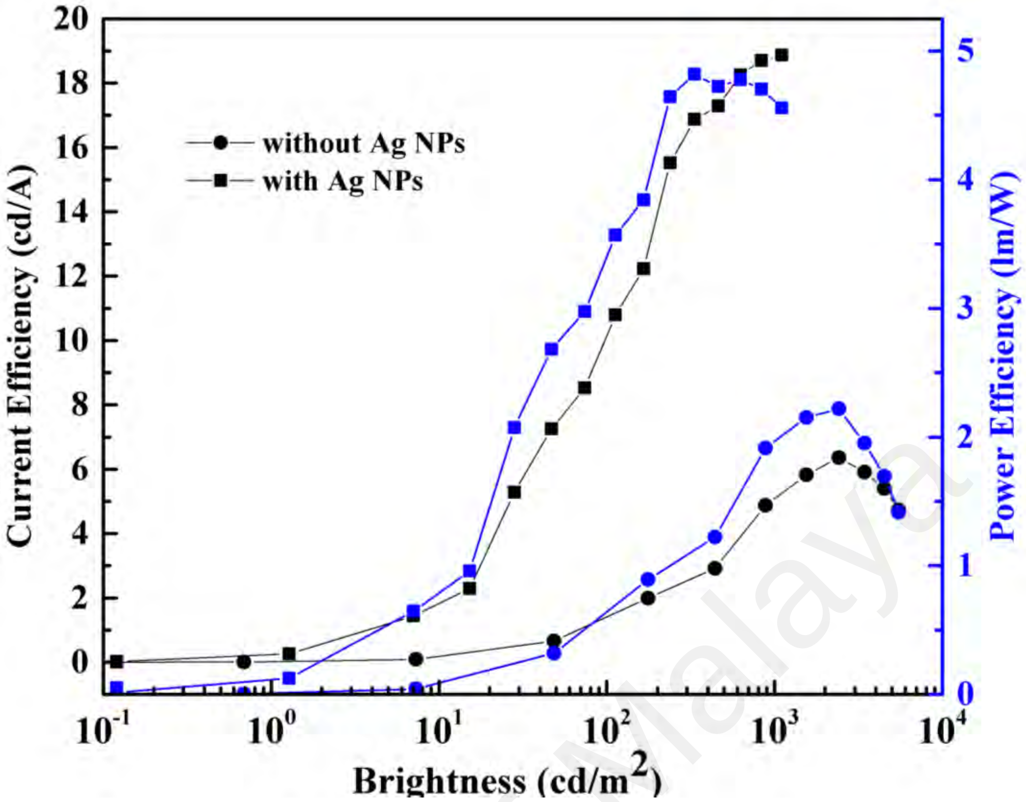

**Figure 5.5:** Device efficiency of OLED device versus the brightness.

### 5.2.3 LSPR peak for Red electrophosphorescent OLED device

Following the enhancement achieved for green OLED, the work continued with the second OLED device based on Iridium (Morfa et al.) bis(2-(2'-benzo-thienyl)pyridinatoN,C3')(acetyl-acetonate) (Ir(piq)$_2$acac) emitter, which is red OLED. Figure 5.6 shows spectra shifting of Ag NPs to ~ 498 nm also covers the PL emission of the Ir(piq)$_2$acac emitter. However, the overlap for these spectra is not at the peak unlike the green emission shown before.

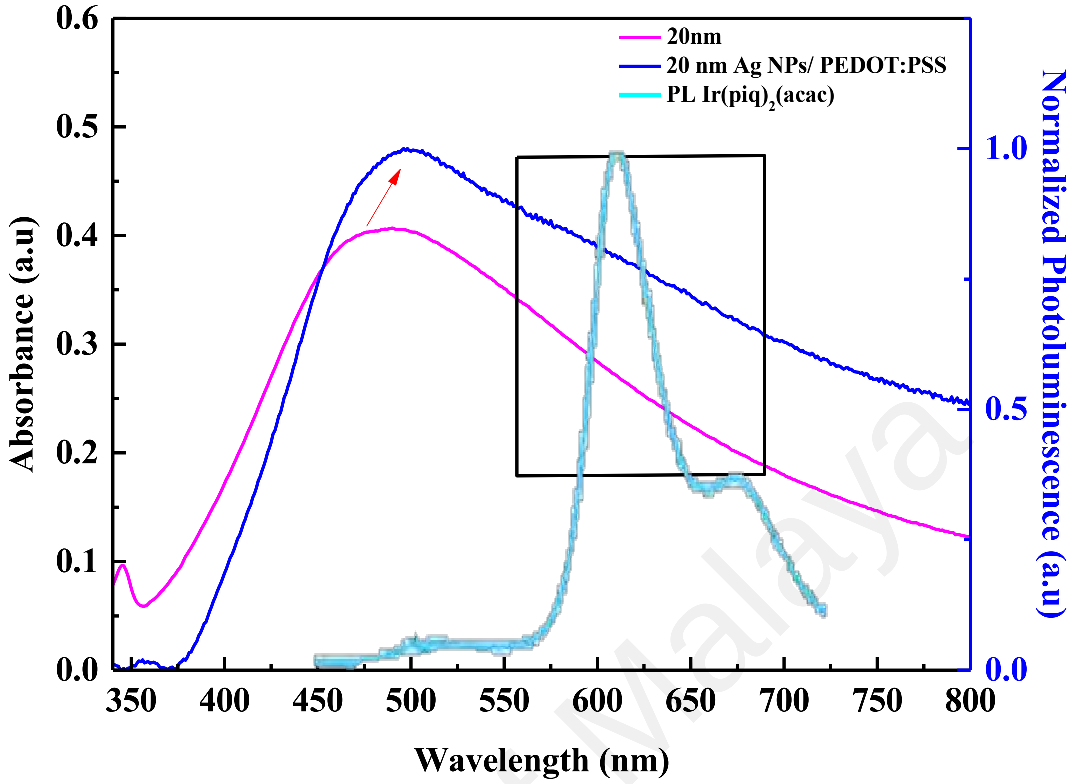

**Figure 5.6:** PL and absorbance spectra of Ir(piq)2acac and Ag NPs respectively.

### 5.2.4 Red electrophosphorescent OLED device efficiency

Figure 5.7 shows the current density of the device with and without Ag NPs for red OLED. It can be seen that Ag NPs device shows the same behavior as the green device, where the device with Ag NPs exhibits lower current density compared to the device without Ag NPs. For example, to get 50 mA, the device without Ag NPs only requires driving voltage of 9.3 V, but the device with Ag NPs needs more than 10.2 V. The same energy level diagram as in Figure 5.4 can be used to explain the hole injection barrier from ITO. The only difference between green and red OLED is the emitter, which does not affect the injection from the anode. This result confirmed the behavior of Ag NPs in OLED inhibit the hole injection into the active layer.

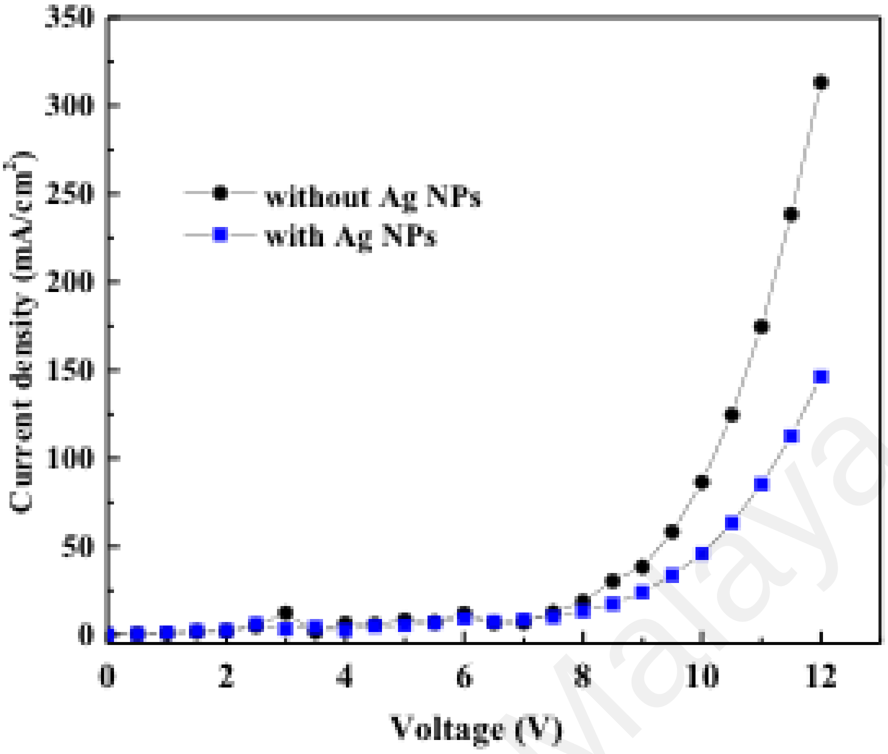

**Figure 5.7:** Current density versus Voltage (J-V) for OLED based Ir(piq)$_2$acac as emitter.

For green device, even though Ag NPs based device exhibits lower current density, the device efficiency for the device with Ag NPs device was enhanced. However, for red device, the device efficiency with Ag NPs shows a poor performance compared to the device without Ag NPs as shown in Figure 5.8. At 1000 cd/m$^2$, the efficiency for the device without Ag NPs is 1.62 cd/A with 0.56 lm/W, while the device with Ag NPs exhibits 0.69 cd/A with 0.18 lm/W for current efficiency and power efficiency respectively. Reducing hole carrier apparently disturb the original charge balance in the device, which is opposite to the green device. This result also indicates that there is no spontaneous emission rate from the plasmonic near-field effect induced by Ag NPs in red OLED.

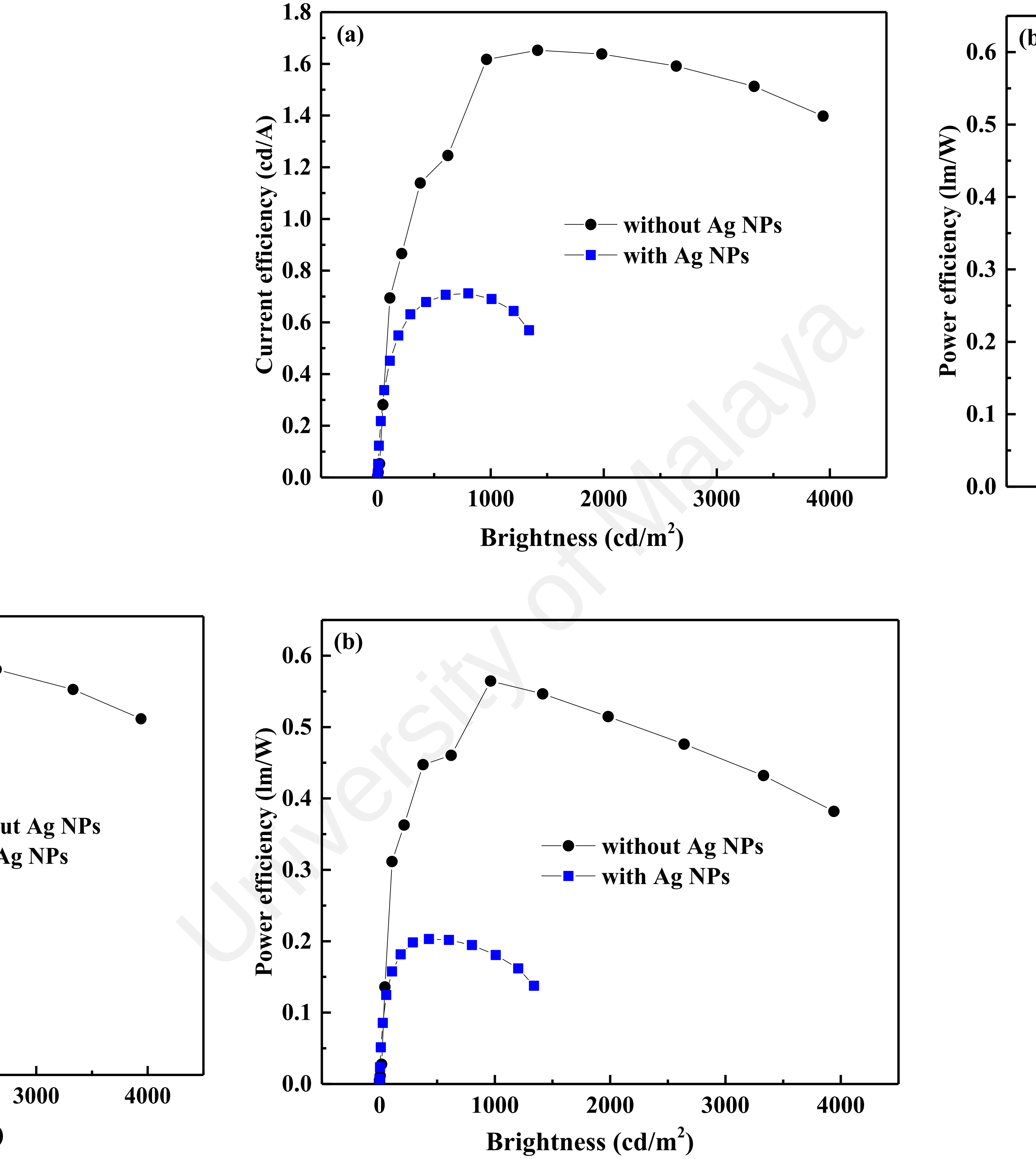

**Figure 5.8:** Device efficiency of OLED device versus the brightness (a) current efficiency and (b) power efficiency.

# CHAPTER 6: CONCLUSION AND SUGGESTION FOR FUTURE WORKS

## 6.1 CONCLUSION

Few different thicknesses of Ag NPs films prepared via electron beam technique with different time of exposure were produced. The influence of temperature used for annealing, the thickness influence on the NPs coalescence, and the effect of layer thickness on surface roughness as well as on the UV-Vis absorption was successfully carried out. The study shows that all these parameters has strongly influence the behavior of the Ag NPs. The experimental results are summarized as follow:

1) FESEM results show morphological studies of Ag nanoparticles (NPs). It could be observed that the shape of Ag NPs changed as the thickness of the Ag NPs layer was varied. Annealing process after deposition induces a surface mass transfer between the nanoparticles resulting the size increases as the film thickness increased. Almost perfect spherical shape produced from 20 nm thin films and gradually transformed into a cluster of an island-like shape for 40 nm thin films. In this experiment, 250 $^{o}$C is the suitable temperature for Ag film because high temperature could cause the significant silver evaporation.
2) AFM shown in our work is consistent with the FESEM result. Mean roughness increase as Ag NPs thickness increase.
3) UV-Vis results reveal that the absorption peak is red-shifted as film thickness increase. The intensity of the peak is gradually increased as the thickness of Ag NPs film increased. This can also attributes to the increasing of particles diameter, which is consistent with the FESEM.

Two different softwares; that are Adaptive Neuro-Fuzzy Inference System (ANFIS) and Finite Domain Time Difference (FDTD) were used to simulate the effect of different parameters and compare it with the experimental results. In addition to that, a model developed using support vector regression (SVR) method was also demonstrated as a prediction of Ag NPs LSPR over a wide range of wavelength. Theoretical experimental results are as follow:

1) The main advantages of the ANFIS scheme include computational efficiency and high flexibility to incorporate optimization and adaptive techniques. ANFIS can also be expanded to systems handling more complex parameters. Further advantages of the ANFIS are its speed of operation, which is much faster than in other control strategies. The root mean square error for the ANFIS network is 0.02061.
2) FDTD results show that there are some trends that can be noticed for up to three film thicknesses where the absorbance peak increases as the film thickness increase. It can be conclude that, the results obtained from FESEM are comparable with calculated results from FDTD.
3) In SVR study, the polynomial and radial basis function (RBF) area applied as the kernel function of Support Vector Regression (SVR) to estimate and predict the LSPR over abroad wavelength range by a process in which the resonance spectra of silver nanoparticles differing in thickness. Instead of minimizing the observed training error, SVR_poly, SVR_rbf and SVR_lin attempt to minimize the generalization error bound to achieve generalized performance. The experimental results show an improvement in predictive accuracy and capability of generalization which can be achieved by the SVR_poly approach in compare to SVR_rbf and SVR_lin methodology. It was found the best testing errors for the SVR_poly approach.

Using the optimum thickness of Ag NPs, the fabrication of the organic light emitting diodes (OLEDs) was carried out where Ag NPs was incorporated as a hole-injection layer (HIL). Two different colors of OLED devices were demonstrated, which are green and red electrophosphorescent. The results are concluded as follow:

1) **Green OLED**

a. Spectra for 20 nm Ag NPs indeed covers the range of Ir(mppy)$_3$ PL emission spectra. The overlap of these two spectra suggests that there might be a possible resonance radiated light generated in Ir(mppy)$_3$ and localized SP excited by Ag NPs.

b. The device with Ag NPs exhibits lower current density compared to the device without Ag NPs. To get 20 mA, the device without Ag NPs only requires driving voltage of 3 V, but the device with Ag NPs needs more than 10 V.

c. Device efficiency for the device with Ag NPs is enhanced. At 1000 cd/m$^2$, the efficiency for the device with Ag NPs is 18.8 cd/A with 4.96 lm/W, while the device without Ag NPs exhibits 5.32 cd/A with 2.04 lm/W for current efficiency and power efficiency respectively. Ag NP's device enhancement is more than 3 folds than that of the device without Ag NPs.

2) **Red OLED**

a. Ag NP's spectra also covers the PL emission of the Ir(piq)$_2$acac emitter.

b. Device with Ag NPs exhibits lower current density compared to the device without Ag NPs. To get 50 mA, the device without Ag NPs only requires driving voltage of 9.3 V, but the device with Ag NPs needs more than 10.2 V.

c. The device efficiency with Ag NPs shows a poor performance compared to the device without Ag NPs. At 1000 cd/m$^2$, the efficiency for the device without Ag NPs is 1.62 cd/A with 0.56 lm/W, while the device with Ag NPs exhibits 0.69 cd/A with 0.18 lm/W for current efficiency and power efficiency respectively.

## 6.2 SUGGESTION FOR FURTHER WORK

In the future, we are planning to explore more on FDTD software. Simulations that will be carried out should cover the absorption of metals nanoparticles for different size and shape. Those results from FDTD will be useful to simulate plasmonics OLED as shown in Figure 6.1 using DEVICE software; which is software that is developed under the same company as FDTD and both software are related to each other.

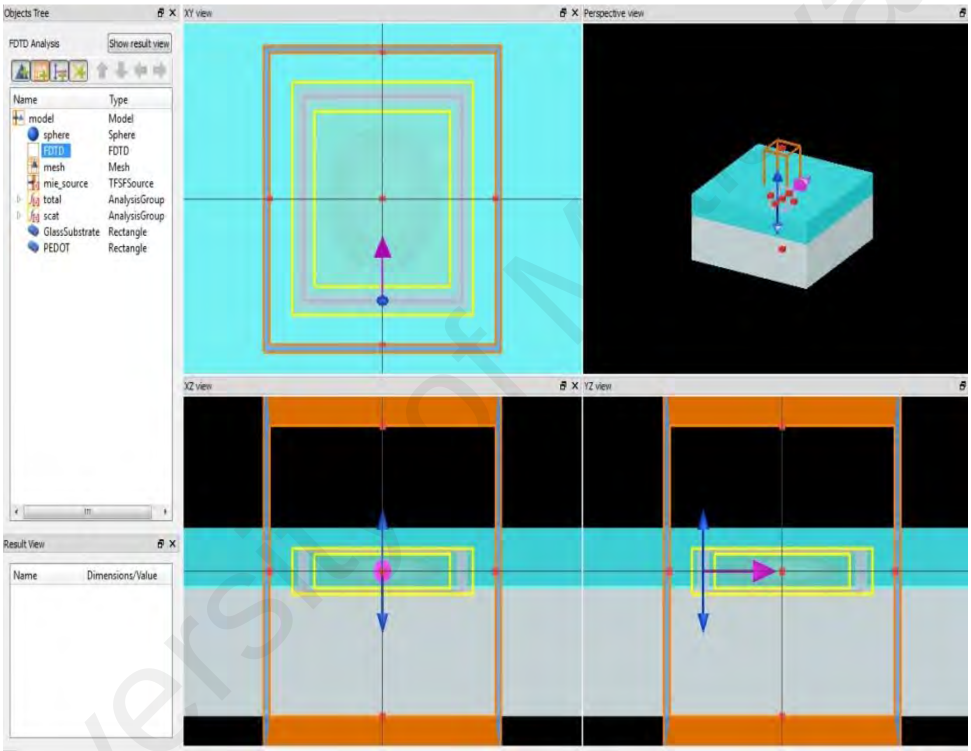

| Name | Type |
|---|---|
| model | Model |
| sphere | Sphere |
| FDTD | FDTD |
| mesh | Mesh |
| mie_source | TFSFSource |
| total | AnalysisGroup |
| scat | AnalysisGroup |
| GlassSubstrate | Rectangle |
| PEDOT | Rectangle |

**Figure 6.1:** OLED device simulated using DEVICE software.

Figures 6.2 and 6.3 show the preliminary results obtained from FDTD where 50 nm Ag nanoparticles are placed in air and on a glass substrate.

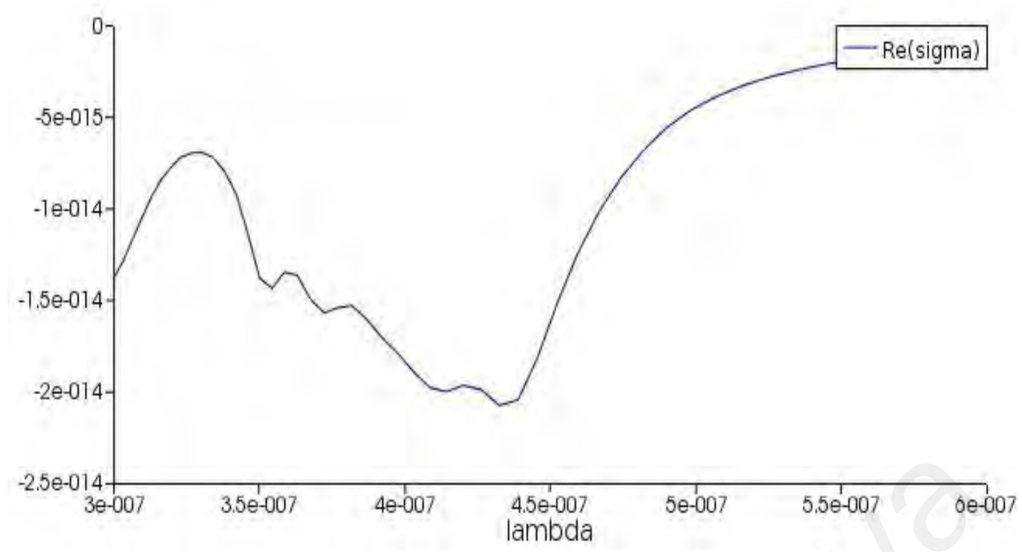

**Figure 6.2:** 50nm Ag NPs in air.

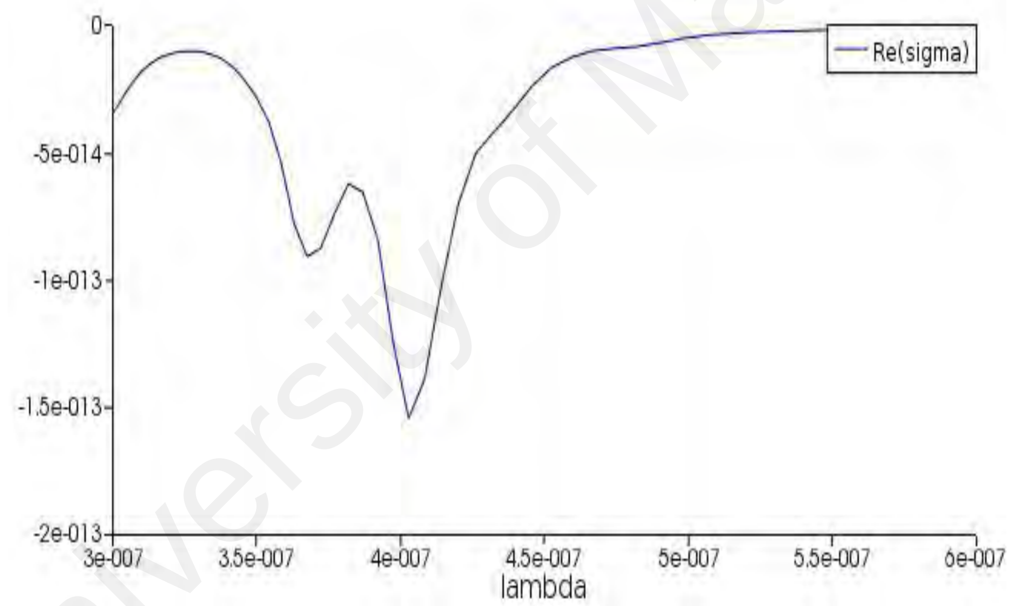

**Figure 6.3:** 50nm Ag NPs array on glass substrate.

We are also planning to optimize distance between the emitting layer and metal nanoparticles as demonstrated in the Figure 6.4 below. Suitable spacer also will be added in the device at certain location to avoid exciton quenching that will produce good efficiency and JV characteristic of OLED device.

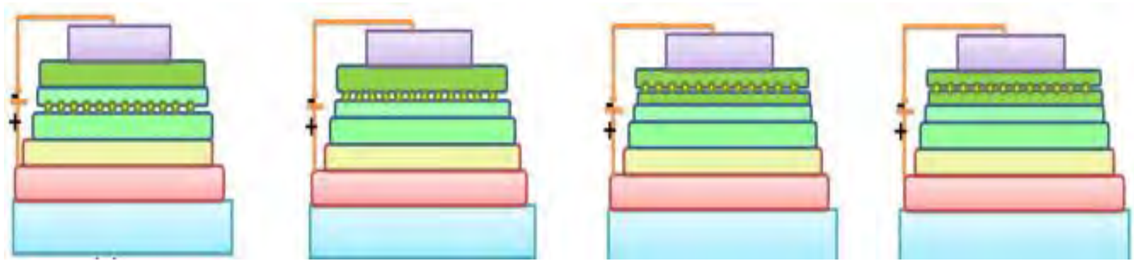

**Figure 6.4:** Different location of metal nanoparticles embedded into the OLED device.

Different shape and size of metal nanoparticle with different techniques will be developed as mention in Chapter 2.

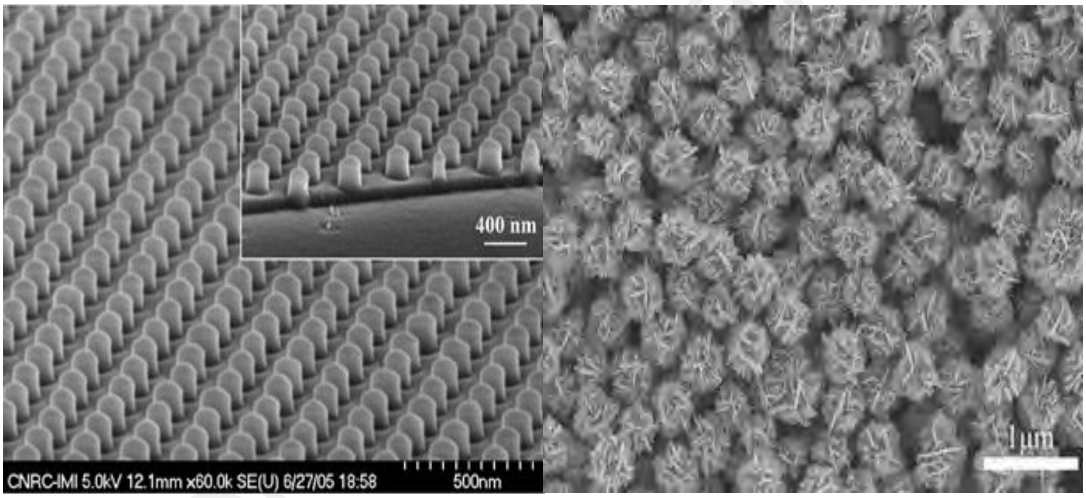

**(a)** **(b)**

**Figure 6.5:** (a) nanodots and (b)nanoflowers

# REFERENCES

Adachi, C., Baldo, M. A., Thompson, M. E. & Forrest, S. R. (2001). Nearly 100% internal phosphorescence efficiency in an organic light-emitting device. *Journal of Applied Physics, 90*, 5048-5051.

Akcayol, M. A. (2004). Application of adaptive neuro-fuzzy controller for SRM. *Advances in Engineering Software, 35*(3), 129-137.

Anatoliy, P., & Uwe, K. (2003). Interface decay cannel of particle surface plasmon resonance. *New Journal of Physics, 5*(1), 151.

Anker, J. N., Hall, W. P., Lyandres, O., Shah, N. C., Zhao, J., & Van Duyne, R. P. (2008). Biosensing with plasmonic nanosensors. *Nature Materials, 7*(6), 442-453.

Atwater, H. A., & Polman, A. (2010). Plasmonics for improved photovoltaic devices. *Nature Material, 9*(3), 205-213.

Atwater, H. A., & Polman, A. (2010). Plasmonics for improved photovoltaic devices. *Nature Materials, 9*(3), 205-213.

Balahur, A., & Turchi, M. (2014). Comparative experiments using supervised learning and machine translation for multilingual sentiment analysis. *Computer Speech & Language, 28*(1), 56-75.

Brütting, W. (2006). *Physics of organic semiconductors*: John Wiley & Sons.

Burroughes, J., Bradley, D., Brown, A., Marks, R., Mackay, K., & Friend, R. (1990). Light-emitting diodes based on conjugated polymers. *Nature, 347*(6293), 539-541.

Catchpole, K., & Polman, A. (2008). Plasmonic solar cells. *Optics Express, 16*(26), 21793-21800.

Chen, X., Jia, B., Saha, J. K., Cai, B., Stokes, N., & Qiao, Q. (2012). Broadband enhancement in thin-film amorphous silicon solar cells enabled by nucleated silver nanoparticles. *Nano letters, 12*(5), 2187-2192.

Cubukcu, E., Zhang, S., Park, Y. -S., Bartal, G., & Zhang, X. (2009). Split ring resonator sensors for infrared detection of single molecular monolayers. *Applied Physics Letters, 95*(4), 043113.

Dahmen, C., Schmidt, B., & von Plessen, G. (2007). Radiation damping in metal nanoparticle pairs. *Nano Letters, 7*(2), 318-322.

Daniel, M. -C., & Astruc, D. (2004). Gold nanoparticles: assembly, supramolecular chemistry, quantum-size-related properties, and applications toward biology, catalysis, and nanotechnology. *Chemical Reviews, 104*(1), 293-346.

Das, M., Hohertz, D., Nirwan, R., Brolo, A. G., Kavanagh, K. L., & Gordon, R. (2011). Improved performance of nanohole surface plasmon resonance sensors by the integrated response method. *IEEE Photonics Journal, 3*(3), 441-449.

Delachat, F., Carrada, M., Ferblantier, G., Grob, J., & Slaoui, A. (2009). properties of silicon nanoparticles embedded in SiNx deposited by microwave-PECVD. *Nanotechnology, 20*(41), 415608.

Eliezer, S., Eliaz, N., Grossman, E., Fisher, D., Gouzman, I., Henis, Z., & Pecker, S. (2004). Synthesis of nanoparticles with femtosecond laser pulses. *Physical Review B, 69*(14), 144119.

Enayatifar, R., Sadaei, H. J., Abdullah, A. H., & Gani, A. (2013). Imperialist competitive algorithm combined with refined high-order weighted fuzzy time series (RHWFTS–ICA) for short term load forecasting. *Energy Conversion and Management, 76*, 1104-1116.

Facchetti, A. (2010). Π-conjugated polymers for organic electronics and photovoltaic cell applications†. *Chemistry of Materials, 23*(3), 733-758.

Farzinpour, P., Sundar, A., Gilroy, K., Eskin, Z., Hughes, R., & Neretina, S. (2012). Altering the dewetting characteristics of ultrathin gold and silver films using a sacrificial antimony layer. *Nanotechnology, 23*(49), 495604.

Félidj, N., Aubard, J., & Lévi, G. (1999). Discrete dipole approximation for ultraviolet–visible extinction spectra simulation of silver and gold colloids. *The Journal of Chemical Physics, 111*(3), 1195-1208.

Ford, G. W., & Weber, W. H. (1984). Electromagnetic interactions of molecules with metal surfaces. *Physics Reports, 113*(4), 195-287.

Freestone, I., Meeks, N., Sax, M., & Higgitt, C. (2007). The lycurgus cup — a roman nanotechnology. *Gold Bulletin, 40*(4), 270-277.

Futamata, M., Maruyama, Y., & Ishikawa, M. (2003). Local electric field and scattering cross section of ag nanoparticles under surface plasmon resonance by finite difference time domain method. *The Journal of Physical Chemistry B, 107*(31), 7607-7617.

Gaspar, D., Pimentel, A. C., Mateus, T., Leitão, J. P., Soares, J., Falcão, B. P., Vicente, A. (2013). Influence of the layer thickness in plasmonic gold nanoparticles produced by thermal evaporation. *Scientific Reports, 3*, 1469. doi: 10.1038/srep01469

Geddes, C. D., & Lakowicz, J. R. (2002). Metal-enhanced fluorescence. *Journal of Fluorescence, 12*(2), 121-129.

Giannini, V., Vecchi, G., & Rivas, J. G. (2010). Lighting up multipolar surface plasmon polaritons by collective resonances in arrays of nanoantennas. *Physical Review Letters, 105*(26), 266801.

Gray, S. K., & Kupka, T. (2003). Propagation of light in metallic nanowire arrays: Finite-difference time-domain studies of silver cylinders. *Physical Review B, 68*(4), 045415.

Grigorie, T., & Botez, R. (2009). Adaptive neuro-fuzzy inference system-based controllers for smart material actuator modelling. *Proceedings of the Institution of Mechanical Engineers, Part G: Journal of Aerospace Engineering, 223*(6), 655-668.

Haiss, W., Thanh, N. T. K., Aveyard, J., & Fernig, D. G. (2007). Determination of size and concentration of gold nanoparticles from UV−Vis spectra. *Analytical Chemistry, 79*(11), 4215-4221. doi: 10.1021/ac0702084

Halas, N. J., Lal, S., Chang, W.-S., Link, S., & Nordlander, P. (2011). Plasmons in strongly coupled metallic nanostructures. *Chemical Review, 111*(6), 3913-3961.

Hao, E., & Schatz, G. C. (2004). Electromagnetic fields around silver nanoparticles and dimers. *The Journal of Chemical Physics, 120*(1), 357-366.

Helfrich, W., & Schneider, W. (1965). Recombination radiation in anthracene crystals. *Physical Review Letters, 14*(7), 229.

Heo, M., Cho, H., Jung, J. W., Jeong, J. R., Park, S., & Kim, J. Y. (2011). High‐performance organic optoelectronic devices enhanced by surface plasmon resonance. *Advanced Materials, 23*(47), 5689-5693.

Huang, X., & El-Sayed, M. A. (2010). Gold nanoparticles: Optical properties and implementations in cancer diagnosis and photothermal therapy. *Journal of Advanced Research, 1*(1), 13-28.

Hulteen, J. C., Treichel, D. A., Smith, M. T., Duval, M. L., Jensen, T. R., & Van Duyne, R. P. (1999). Nanosphere lithography: size-tunable silver nanoparticle and surface cluster arrays. *The Journal of Physical Chemistry B, 103*(19), 3854-3863.

Jain, P. K., Eustis, S., & El-Sayed, M. A. (2006). Plasmon coupling in nanorod assemblies: optical absorption, discrete dipole approximation simulation, and exciton-coupling model. *The Journal of Physical Chemistry B, 110*(37), 18243-18253.

Jain, P. K., Huang, W., & El-Sayed, M. A. (2007). On the universal scaling behavior of the distance decay of plasmon coupling in metal nanoparticle pairs: A plasmon ruler equation. *Nano Letters, 7*(7), 2080-2088.

Jain, P. K., Huang, X., El-Sayed, I. H., & El-Sayed, M. A. (2007). Review of some interesting surface plasmon resonance-enhanced properties of noble metal nanoparticles and their applications to biosystems. *Plasmonics, 2*(3), 107-118.

Jain, P. K., Lee, K. S., El-Sayed, I. H., & El-Sayed, M. A. (2006). Calculated absorption and scattering properties of gold nanoparticles of different size, shape, and composition: Applications in biological imaging and biomedicine. *The Journal of Physical Chemistry B, 110*(14), 7238-7248.

Javanmardi, S., Shojafar, M., Amendola, D., Cordeschi, N., Liu, H., & Abraham, A. (2014). *Hybrid job scheduling algorithm for cloud computing environment.* Paper presented at the Proceedings of the Fifth International Conference on Innovations in Bio-Inspired Computing and Applications IBICA 2014.

Kelly, K. L., Coronado, E., Zhao, L. L., & Schatz, G. C. (2003). The optical properties of metal nanoparticles:  The influence of size, shape, and dielectric environment. *The Journal of Physical Chemistry B, 107*(3), 668-677.

Khoshnevisan, B., Rajaeifar, M. A., Clark, S., Shamahirband, S., & Anuar, N. B. (2014). Evaluation of traditional and consolidated rice farms in guilan province, iran, using life cycle assessment and fuzzy modeling. *Science of the Total Environment, 481*, 242-251.

Kim, H. S., Kim, C. K., & Jang, H. W. (2013). Fabrication of a microball lens array for OLEDs fabricated using a monolayer microsphere template. *Electronic Materials Letters, 9*(1), 39-42.

Kim, J. H., Cho, J.-Y., Park, J., Lee, B. K., & Baek, K.-H. (2014). Improvement of light out-coupling efficiency in organic light-emitting diodes with variable nanopatterns. *Electronic Materials Letters, 10*(1), 27-29.

Kim, Y. T., Han, J. H., Hong, B. H., & Kwon, Y. U. (2010). Electrochemical synthesis of cdse quantum-dot arrays on a graphene basal plane using mesoporous silica thin ‐ film templates. *Advanced Materials, 22*(4), 515-518.

Kochuveedu, S. T., & Kim, D. H. (2014). Surface plasmon resonance mediated photoluminescence properties of nanostructured multicomponent fluorophore systems. *Nanoscale, 6*(10), 4966-4984.

Kreibig, U. (1986). Systems of small metal particles: optical properties and their structure dependences. *Zeitschrift für Physik D Atoms, Molecules and Clusters, 3*(2), 239-249.

Kreibig, U., & Vollmer, M. (2013). *Optical properties of metal clusters* (Vol. 25). Springer Science & Business Media.

Kühn, S., Håkanson, U., Rogobete, L., & Sandoghdar, V. (2006). Enhancement of single-molecule fluorescence using a gold nanoparticle as an optical nanoantenna. *Physical Review Letters, 97*(1), 017402.

Kulkarni, A. P., Noone, K. M., Munechika, K., Guyer, S. R., & Ginger, D. S. (2010). Plasmon-enhanced charge carrier generation in organic photovoltaic films using silver nanoprisms. *Nano Letters, 10*(4), 1501-1505.

Kumar, A., Srivastava. R., Mehta, D. S. & Kamalasanan, M. N. (2012). Surface plasmon enhanced blue organic light emitting diode with nearly 100% fluorescence efficiency. *Organis Electronics,  13*(9), 1750-1755.

Kumar, A., Srivastava, R., Tyagi, P., Mehta, D. S., & Kamalasanan, M. N. (2012). Efficiency enhancement of organic light emitting diode via surface energy transfer between exciton and surface plasmon. *Organic Electronics, 13*(1), 159-165.

Lassiter, J. B., Aizpurua, J., Hernandez, L. I., Brandl, D. W., Romero, I., Lal, S., & Halas, N. J. (2008). Close encounters between two nanoshells. *Nano Letters, 8*(4), 1212-1218.

Law, W. -C., Yong, K. -T., Baev, A., & Prasad, P. N. (2011). Sensitivity improved surface plasmon resonance biosensor for cancer biomarker detection based on plasmonic enhancement. *ACS Nano, 5*(6), 4858-4864.

Linic, S., Christopher, P., & Ingram, D. (2011). Plasmonic-metal nanostructures for efficient conversion of solar to chemical energy. *Nature Materials, 10*(12), 911-921.

Liu, F., & Nunzi, J. -M. (2012). Enhanced organic light emitting diode and solar cell performances using silver nano-clusters. *Organic Electronics, 13*(9), 1623-1632.

Madigan, C. F., Lu, M.-H., & Sturm, J. C. (2000). Improvement of output coupling efficiency of organic light-emitting diodes by backside substrate modification. *Applied Physics Letters, 76*(13), 1650-1652.

Meerheim, R., Nitsche, R., & Leo, K. (2008). High-efficiency monochrome organic light emitting diodes employing enhanced microcavities. *Applied Physics Letters, 93*(4), 281.

Mendes, P. M., Jacke, S., Critchley, K., Plaza, J., & Fitzmaurice, D. (2004). Gold nanoparticle patterning of silicon wafers using chemical ebeam lithography. *Langmuir, 20*(9), 3766-3768.

Morfa, A. J., Rowlen, K. L., Reilly III, T. H., Romero, M. J., & Van de Lagemaat, J. (2008). Plasmon-enhanced solar energy conversion in organic bulk heterojunction photovoltaics. *Applied Physics Letters, 92*(1), 013504.

Mulvaney, P. (1996). Surface plasmon spectroscopy of nanosized metal particles. *Langmuir, 12*(3), 788-800.

Nijmegen, R. U. (2014). *How does em work*. Retrived from http://www.vcbio.science.ru.nl/en/fesem/info/principe/

Yeshchenko, O. A., Dmitruk, I. M., Alexeenko, A. A., Losytskyy, Y. M., Kotko, A.V., and Pinchuk, A.O. (2009). Size-dependent surface-plasmon-enhanced photoluminescence from silver nanoparticles embedded in silica. *Physical Review B, 79*, 235438.

Oubre, C., & Nordlander, P. (2004). Optical properties of metallodielectric nanostructures calculated using the finite difference time domain method. *The Journal of Physical Chemistry B, 108*(46), 17740-17747.

Perner, M., Bost, P., Lemmer, U., Von Plessen, G., Schmitt, M., & Schmidt, H. (1997). Optically induced damping of the surface plasmon resonance in gold colloids. *Physical Review Letters, 78*(11), 2192.

Pooranian, Z., Shojafar, M., Abawajy, J. H., & Abraham, A. (2015). An efficient meta-heuristic algorithm for grid computing. *Journal of Combinatorial Optimization, 30*(3), 413-434.

Pope, M., Kallmann, H., & Magnante, P. (1963). Electroluminescence in organic crystals. *The Journal of Chemical Physics, 38*(8), 2042-2043.

Rajasekaran, S., Gayathri, S., & Lee, T.-L. (2008). Support vector regression methodology for storm surge predictions. *Ocean Engineering, 35*(16), 1578-1587.

Ru, E. L., & Etchegoin, P. (2009). *Principles of surface enhanced raman spectroscopy*. Oxford: Elsevier.

Rycenga, M., Cobley, C. M., Zeng, J., Li, W., Moran, C. H., Zhang, Q., & Xia, Y. (2011). Controlling the synthesis and assembly of silver nanostructures for plasmonic applications. *Chemical Reviews, 111*(6), 3669-3712.

Schwoerer, M., & Wolf, H. C. (2007). *Organic molecular solids*: John Wiley & Sons.

Shah, S., Li, W., Huang, C.-P., Jung, O., & Ni, C. (2002). Study of Nd3+, Pd2+, Pt4+, and Fe3+ dopant effect on photoreactivity of $TiO_2$ nanoparticles. *Proceedings of the National Academy of Sciences 99*(suppl 2), 6482-6486.

Skrabalak, S. E., Au, L., Lu, X., Li, X., & Xia, Y. (2007). Gold nanocages for cancer detection and treatment. *Nanomedicine*, *2*(5), 657-668.

Sun, S., Mendes, P., Critchley, K., Diegoli, S., Preece, J. A., & Richardson, T. H. (2006). Fabrication of gold micro-and nanostructures by photolithographic exposure of thiol-stabilized gold nanoparticles. *Nano Letters, 6*(3), 345-350.

Tang, C. W., & VanSlyke, S. A. (1987). Organic electroluminescent diodes. *Applied Physics Letters, 51*(12), 913-915.

Tanyeli, I., Nasser, H., Es, F., Bek, A., & Turan, R. (2013). Effect of surface type on structural and optical properties of ag nanoparticles formed by dewetting. *Optics Express, 21*(S5), A798-A807. doi: 10.1364/oe.21.00a798

Tesler, A. B., Chuntonov, L., Karakouz, T., Bendikov, T. A., Haran, G., Vaskevich, A., & Rubinstein, I. (2011). Tunable localized plasmon transducers prepared by thermal dewetting of percolated evaporated gold films. *The Journal of Physical Chemistry C, 115*(50), 24642-24652.

Thompson, C. V. (2012). Solid-state dewetting of thin films. *Annual Review of Materials Research, 42*(1), 399-434.

Tiwari, J. N., Tiwari, R. N., & Kim, K. S. (2012). Zero-dimensional, one-dimensional, two-dimensional and three-dimensional nanostructured materials for advanced electrochemical energy devices. *Progress in Materials Science, 57*(4), 724-803.

Vollmer, M. & Krebig, U. (1995). *Optical properties of metal clusters*. Berlin.

Wang, H., Tam, F., Grady, N. K., & Halas, N. J. (2005). Cu nanoshells: Effects of interband transitions on the nanoparticle plasmon resonance. *The Journal of Physical Chemistry B, 109*(39), 18218-18222.

Wikibooks. (2013). Nanotechnology. Retrived from https://en.wikibooks.org/w/index.php?title=Nanotechnology&oldid=2590553.

Williams, D., & Schadt, M. (1970). A simple organic electroluminescent diode. *Proceedings of the IEEE, 58*(3), 476-476.

Xiao, Y., Yang, J., Cheng, P., Zhu, J., & Xu, Z. (2012). Surface plasmon-enhanced electroluminescence in organic light-emitting diodes incorporating Au nanoparticles. *Applied Physics Letters, 100*(1), 8.

Yang, H., Huang, K., King, I., & Lyu, M. R. (2009). Localized support vector regression for time series prediction. *Neurocomputing, 72*(10), 2659-2669.

Yersin, H. (2004). Triplet emitters for OLED applications. Mechanisms of exciton trapping and control of emission properties. *Transition Metal and Rare Earth Compounds* (pp. 1-26): Springer.

Zakaria, R., Che Noh, S. M., Petković, D., Shamshirband, S., & Penny, R. (2014). Investigation of plasmonic studies on morphology of deposited silver thin films having different thicknesses by soft computing methodologies - A comparative study. *Physica E: Low-dimensional Systems and Nanostructures, 63*, 317-323.

Zakaria, R., Lin, W. K., & Lim, C. C. (2012). Plasmonic enhancement of gold nanoparticles in poly (3-hexylthiophene) organic phototransistor. *Applied Physics Express, 5*(8), 082002.

Zhang, G., & Wang, D. (2009). Colloidal lithography the art of nanochemical patterning. *Chemistry An Asian Journal, 4*(2), 236-245.

Zhang, L., Zhou, W. -D., Chang, P. -C., Yang, J. -W., & Li, F. -Z. (2013). Iterated time series prediction with multiple support vector regression models. *Neurocomputing, 99*, 411-422.

# LIST OF PUBLICATIONS AND CONFERENCE

## Published paper:

1. **Munirah, S.,** Shamshirband, S., Petković, D., Penny, R., & Zakaria, R. (2014). Adaptive neuro-fuzzy appraisal of plasmonic studies on morphology of deposited silver thin films having different thicknesses. *Plasmonics*, 9, 1189–1196.

2. Zakaria, R., **Munirah, S.,** Petković, D., Shamshirband, S., & Penny, R. (2014). Investigation of plasmonic studies on morphology of deposited silver thin films having different thicknesses by soft computing methodologies-A comparative study. *Physica E, 63,* 317-323.

3. Zakaria, R., Hamdan, K. S., **Che Noh, S. M**., Supangat, A., & Sookhakian, M. (2015). Surface plasmon resonance and photoluminescence studies of Au and Ag micro-flowers. *Optical Material*. Online access from http://repository.um.edu.my/98457/1/RozalinaZakaria2015.pdf

## Attended conference:

1. The 8th Mathematics and Physical Sciences Graduate Congress (MPSGC), 8th – 10th December 2012, Chulalongkorn University, Bangkok, Thailand.